

# Constraining alternative theories of gravity by gravitational waves from precessing eccentric compact binaries with LISA

Kent Yagi<sup>1</sup> and Takahiro Tanaka<sup>2</sup>

<sup>1</sup>*Department of Physics, Kyoto University, Kyoto, 606-8502, Japan*

<sup>2</sup>*Yukawa Institute for Theoretical Physics, Kyoto University, Kyoto 606-8502, Japan*

## Abstract

We calculate how strongly one can put constraints on the alternative theories of gravity such as Brans-Dicke and massive graviton theories with LISA. We consider the inspiral gravitational waves from NS/IMBH binaries in Brans-Dicke theory and SMBH/BH binaries in massive graviton theories. We use the 2PN waveforms including spins. We also take both precession and small eccentricity of the orbit into account. We neglect the spin of one of the binary object so that we can apply the so-called *simple precession*. We perform the Monte Carlo simulations of  $10^4$  binaries, estimating the determination accuracy of binary parameters including  $\omega_{\text{BD}}$  and  $\lambda_g$  for each binary using the Fisher matrix method. We find that including both the spin-spin coupling  $\sigma$  and the small eccentricity into the binary parameters reduces the determination accuracy by an order of magnitude for the Brans-Dicke case, whilst it has less influence on massive graviton theories. On the other hand, including precession enhances the constraint on  $\omega_{\text{BD}}$  only 20% but it increases the constraint on  $\lambda_g$  by several factors. For  $(1.4 + 1000)M_\odot$  NS/BH binaries of  $\text{SNR}=\sqrt{200}$ , one can put  $\omega_{\text{BD}} > 7040$ , whilst for  $(10^7 + 10^6)M_\odot$  BH/BH binaries at 3Gpc, one can put  $\lambda_g > 4.24 \times 10^{21}\text{cm}$ , on average. This is four orders of magnitude stronger than the one obtained from the solar system experiment. From these results, it is understood that the effects of precession and eccentricity cannot be neglected in the parameter estimation analysis.

## 1 INTRODUCTION

Recent observations (e.g. type Ia SNe [1]) show that the expansion of our universe is accelerating at the moment. However, no one knows the origin of this expansion. One possibility to solve this problem is to introduce some undiscovered matter field such as quintessence or k-essence (for a recent review, see [2]). Another possibility is to modify gravitational theory from general relativity. The easiest modification is to add some scalar degrees of freedom to gravity. This type of theory is called the scalar-tensor theory [3]. This theory also appears to be a candidate for solving the inflation problem, known as the hyper-extended inflation [4]. Furthermore, this theory may arise in the context of the string theory, which contains some scalar fields called the dilatons and the moduli. Therefore it is very important to put strong observational constraint on this theory. In this paper, we focus on Brans-Dicke theory [5], which is the simplest scalar-tensor theory. This theory has the so-called Brans-Dicke parameter  $\omega_{\text{BD}}$  and by taking the limit  $\omega_{\text{BD}} \rightarrow \infty$ , it reduces to general relativity. The current strongest constraint is  $\omega_{\text{BD}} > 40000$ , which is obtained from the solar system experiment, measuring the Shapiro time delay using the Saturn probe satellite Cassini [6].

Another type of modified theory of gravity introduces a finite mass to a graviton. This type of theory is called the massive graviton theory (e.g. Fierz-Pauli theory [7] and DGP braneworld scenario [8]). Therefore it is also important to put constraint on the graviton mass (or the graviton Compton wavelength  $\lambda_g \equiv h/m_g c$ ). When the graviton is massive, the gravitational potential is modified from Newtonian to Yukawa type. Then, the effective gravitational constant depends on the distance from the gravitational source, which changes the Kepler's third law from Newtonian. Verification of this third law in the solar system experiment puts the lower bound on the Compton wavelength as  $\lambda_g > 2.8 \times 10^{17}\text{cm}$ .

<sup>1</sup>E-mail:kent@tap.scphys.kyoto-u.ac.jp

<sup>2</sup>E-mail:tanaka@yukawa.kyoto-u.ac.jp

In this paper, we estimate the possible constraint we can get on  $\omega_{\text{BD}}$  and  $\lambda_g$  by detecting gravitational waves from the inspiral of precessing eccentric compact binaries with LISA [9, 10]. The constraint on  $\omega_{\text{BD}}$  using binary gravitational waves was first discussed by Eardley [11]. In Brans-Dicke theory, the additional scalar field contains the dipole radiation [12, 13]. This modifies the binary's orbital evolution from the one in general relativity. Eardley mentioned that it is possible to constrain  $\omega_{\text{BD}}$  by measuring the rate of the secular decrease in the orbital period. The change in the orbital evolution due to this dipole radiation modifies the phasing of the gravitational waveform. Will [14] applied the matched filtering analysis and calculated how accurately one can determine the binary parameters including  $\omega_{\text{BD}}$  using advanced LIGO. Scharre and Will [15] and Will and Yunes [16] did the same analysis using LISA. However, these calculations do not include binary spins and also they used the pattern-averaged waveforms (having been averaged over the source direction  $(\theta_s, \phi_s)$  and the direction of the orbital angular momentum  $(\theta_L, \phi_L)$ ). Berti *et al.* [17] calculated the determination errors including the effect of the spin-orbit coupling using LISA. Also, they performed the Monte Carlo simulations in which they randomly distribute  $10^4$  sources over the sky, calculate the constraint on  $\omega_{\text{BD}}$  from each binary and take the average at the end. According to their analysis, for  $(1.4+1000)M_\odot$  NS/BH binary of  $\text{SNR}=\sqrt{200}$ , 1 year observation by LISA can put the bound  $\omega_{\text{BD}} > 10799$  on average.

In massive graviton theories, the propagation speed of gravitational wave depends on its frequency, which modifies the time of arrival from general relativity. This also affects the phasing of the gravitational waveforms. Will [18] included  $\lambda_g$  into the binary parameters and carried out the matched filtering analysis, investigating how accurately one can determine  $\lambda_g$  using advanced LIGO or LISA. Will and Yunes [16] did the same analysis using the improved noise curve for LISA. Again, they did not include the effect of binary spins and also they used the pattern-averaged waveforms. Berti *et al.* [17] estimated the constraint on  $\lambda_g$  by performing the Monte Carlo simulations including the additional parameters of the spin-orbit coupling  $\beta$  and the angles  $\theta_s, \phi_s, \theta_L$  and  $\phi_L$ . According to their analysis, for  $(10^6 + 10^6)M_\odot$  BH/BH binary at 3Gpc, 1 year observation by LISA can put the bound  $\lambda_g > 1.33 \times 10^{21}\text{cm}$  on average.

In this paper, we improve the analysis of Ref. [17] by taking the following effects into account: (i) the spin-spin coupling (ii) the small eccentricity (iii) the spin precession. (i) The spin-spin coupling  $\sigma$  appears at 2PN order in the PN waveforms. Berti *et al.* reported that when they included both  $\sigma$  and  $\omega_{\text{BD}}$  or  $\lambda_g$  into parameters, they could not take the inverse of the Fisher matrix properly, because the ratio of the maximum eigenvalue to the minimum one of this matrix approaches the bound for the double precision computation. Hence, we carried out our analysis in the quadruple precision. (ii) As the binary radiates gravitational waves, it loses its energy and angular momentum [19]. Since this circularises the orbit as  $e \propto f^{-19/18}$ , usually the eccentricity is neglected in the analysis. We estimate how much the error of each parameter increases when we add the eccentricity ( $e_0^2$  to be precise, where  $e_0$  is the eccentricity at some specific frequency  $f_0$ ) into the binary parameters. (iii) When the spin of the binary object is not zero, usually the spin-orbit effect and the spin-spin effect cause the spin vectors  $\mathbf{S}_i$  ( $i=1,2$ ) and the orbital angular momentum vector  $\mathbf{L}$  to precess. The parameter estimation errors including effects of precession in general relativity have been calculated by several authors [20, 21, 22, 23, 24, 25]. Vecchio [20] performed the Monte Carlo simulations of equal mass BH/BH binaries with LISA, taking only the leading spin-orbit terms in the precession equations. In this case, the precession equations can be solved analytically up to some appropriate order. This is called the *simple precession* [26]. It has the property that  $\mathbf{L}$  and  $\mathbf{S}_i$  precess around a fixed vector  $\mathbf{J}_0$  which is almost the same as the total angular momentum vector  $\mathbf{J}$ . Another property is that the following three quantities,  $\hat{\mathbf{L}} \cdot \hat{\mathbf{S}}, \hat{\mathbf{S}}_1 \cdot \hat{\mathbf{S}}_2$  and  $S$ , become constant, where  $\mathbf{S} = \mathbf{S}_1 + \mathbf{S}_2$  is the total spin angular momentum and  $S$  is its magnitude. Lang and Hughes [21] solved the full precession equations, which include both spins of the binary stars, numerically and performed the Monte Carlo simulations of super massive BH/BH binaries with LISA. For  $(10^7 + 10^6)M_\odot$  binaries at  $z = 1$ , they found that the determination accuracy for  $\Delta\mu/\mu$  increases by more than two orders of magnitude. Van der Sluys *et al.* [22, 23, 24] performed the Markov Chain Monte Carlo simulations for ground-based detectors, taking the simple precession into account and performed the analysis that is beyond the Fisher matrix method. In Ref. [25], they used the modeled gravitational wave signal injected into LIGO data so that the detector noise they used is more realistic than the Gaussian one. The precession gives some additional information to the waveform, which degenerates the parameter correlations and enhances the parameter determination accuracy. Here, we estimate how much the effect of precession enhances the determination accuracy in alternative theories of gravity. We

assume that the spin of one of the binary objects can be neglected so that the analytic expressions in the simple precession [20] can be applied. The so-called Thomas precession is neglected in Ref. [20] for the computational reasons but we found that this cannot be neglected when the precessing binary becomes  $\hat{\mathbf{L}} \cdot \hat{\mathbf{N}} \approx \pm 1$ , where  $\hat{\mathbf{N}}$  is the unit vector in the direction of the binary. For this reason, we approximately take this Thomas precession into account. Neglecting the spin of NS is justified from observations [27].

Following the analysis of Berti *et al.* [17], we assume that we detect gravitational waves from inspiral compact binaries from 1 year before the coalescences with LISA. We carry out the following Monte Carlo simulations. We distribute  $10^4$  binaries over the sky and estimate the determination accuracy of binary parameters including  $\omega_{\text{BD}}$  and  $\lambda_g$  for each binary using the Fisher matrix method. We take the average at the end. For the LISA noise curve, we use the same analytical approximation presented in [29].

We first performed our analysis using the pattern averaged waveform. For the error estimation in Brans-Dicke theory, the inclusions of both  $\sigma$  and  $e_0^2$  into parameters reduce the determination accuracy by an order of magnitude. Especially, including  $e_0^2$  affects the estimation more than just including  $\sigma$ . However, we found that if we impose the prior  $\Delta e_0^2 > 0$ , the constraint on  $\omega_{\text{BD}}$  would be the same as the one without including  $e_0^2$  into parameters. For analysis in massive graviton theories, the inclusions of these parameters only change the results by a factor of a few. In this case, the inclusion of  $\sigma$  affects more than the inclusion of  $e_0^2$ . Also, the prior on  $e_0^2$  does not affect the result in the massive graviton theories. Next, we performed the Monte Carlo simulations including precession. We found that in Brans-Dicke case, the results are not so much affected by taking precession into account. For NS/BH binaries of  $(1.4 + 1000)M_\odot$  with  $\text{SNR} = \sqrt{200}$ , estimation with taking all  $\sigma$ ,  $e_0^2$  and precession into account can constrain  $\omega_{\text{BD}} > 1196$  on average. However, in the case of massive graviton theories, inclusion of precession has more remarkable effect. For BH/BH binaries of  $(10^7 + 10^6)M_\odot$  at 3Gpc, estimation with taking all  $\sigma$ ,  $e_0^2$  and precession into account can constrain  $\lambda_g > 4.24 \times 10^{21}\text{cm}$  on average. This constraint is 3 times stronger than the result obtained in Ref. [17].

The organisation of this paper is as follows. In Sec. 2, we review the waveforms of the inspiral compact binaries in alternative theories of gravity. Notice the contributions of the gravitational dipole radiation and the change in the propagation speed on  $df/dt$ . In Sec. 3, we discuss the waveform output of the detectors. They are the superposition of the two polarised waves. We consider the case of using two detectors and show the Fourier component of the restricted 2PN waveforms. Section 4 discusses the effect of precession. In Sec. 4.1, we review how the angular momentum vectors  $\mathbf{L}$  and  $\mathbf{S}_i$  precess under the simple precession. In Sec. 4.2, we discuss how the detector output expressed in Sec. 3 changes when the orbital angular momentum  $\mathbf{L}$  evolves with time. We also show how we treat the so-called *Thomas precession*. In Sec. 5, we discuss how to estimate the determination errors of binary parameters using the matched filtering analysis. In Sec. 6, we present the noise curve of LISA that is needed when calculating the Fisher matrix. In Sec. 7, we present the setups and the results of our numerical calculations. In Sec. 7.1.1, we use the pattern-averaged waveforms so that the angles  $\theta_S, \phi_S, \theta_L, \phi_L$  are not taken into parameters. In Sec. 7.1.2, we perform the Monte Carlo simulations of  $10^4$  binaries distributed over the sky. We calculate the determination errors for each binary and take the average. In Sec. 7.2, we carry out the same Monte Carlo simulations including the effect of the simple precession. In Sec. 8, we summarise our main results and discuss some future works.

Just after we have completed our analysis, there appeared a paper by Stavridis and Will [28], in which they estimated the possible bound on graviton mass from SMBH/BH inspiral gravitational waves using LISA. Following Lang and Hughes [21], they randomly included the spins of both binary objects and solved the precession equations numerically. They took spin-spin coupling  $\sigma$  into account but they did not include eccentricity into parameters. For BH/BH binaries of  $(10^6 + 10^6)M_\odot$  at 3Gpc, they obtained the lower bound of  $\lambda_g$  as  $\lambda_g > 5 \times 10^{21}\text{cm}$  which is consistent with our results. Since the binary masses are different between our calculation and their one, we cannot directly compare two results but it seems that inclusion of both spins may affect the results by a factor of a few.

## 2 BINARY GRAVITATIONAL WAVEFORMS IN ALTERNATIVE THEORIES OF GRAVITY

First, we calculate the gravitational waves coming from a binary system of inspiral compact objects in Brans-Dicke theory and massive graviton theories [17]. As this binary radiates gravitational waves, the orbit gets circularised. Because we assume the observation starts 1year before coalescence, we take the eccentricity of this binary orbit as considerably small. Therefore, we only include the leading term for the eccentricity in the phasing part.

On deriving the waveform, we use the post-Newtonian formalism, an expansion in internal gravitational potential  $U$  and  $v^2$  where  $v$  is the internal source velocity. The emitted gravitational waves are the superposition of harmonics at multiples of the orbital period. The waveform  $h(t)$  can be written schematically as

$$h(t) = \text{Re} \left( \sum_{n,m} h_m^n(t) e^{im\phi_{\text{orb}}(t)} \right), \quad (1)$$

where  $n$  labels PN order and  $m$  is an index of the harmonics [30].  $\phi_{\text{orb}} = \int^t \Omega(t') dt'$  is the orbital phase, where  $\Omega(t)$  is the orbital angular velocity. In this paper, we use the “restricted 2PN waveform”. For the amplitude, we only take the leading Newtonian quadrupole term  $h_2^0$ , and for the phase part, we use  $\phi_{\text{orb}}(t)$  up to 2PN order. This is because the correlation between two waveforms is much more sensitive to the phase information than to the amplitude when we perform the matched filtering analysis. In this approximation, the waveforms of  $+$  and  $\times$  polarisations are

$$h_+(t) = A_+ \cos \phi(t), \quad (2)$$

$$h_\times(t) = A_\times \sin \phi(t), \quad (3)$$

where  $\phi(t) = 2\phi_{\text{orb}}(t)$  and

$$A_+ = \frac{2m_1 m_2}{r D_L} (1 + (\hat{\mathbf{L}} \cdot \hat{\mathbf{N}})^2), \quad (4)$$

$$A_\times = -\frac{4m_1 m_2}{r D_L} (\hat{\mathbf{L}} \cdot \hat{\mathbf{N}}). \quad (5)$$

$m_1, m_2$  are the two masses,  $r$  is their orbital separation,  $D_L$  is the luminosity distance between the source and observer,  $\hat{\mathbf{L}}$  is the unit vector parallel to the orbital angular momentum and  $\hat{\mathbf{N}}$  is the unit vector pointing toward the centre of mass of the binary. Please see Appendix B for more explanations on polarisations.

Next, we need to calculate the phase  $\phi(t)$ . First, we introduce the following useful mass parameters;

$$M \equiv m_1 + m_2, \quad (6)$$

$$\mu \equiv \frac{m_1 m_2}{M}, \quad (7)$$

$$\eta \equiv \frac{\mu}{M}, \quad (8)$$

$$\mathcal{M} \equiv \mu^{3/5} M^{2/5} = M \eta^{3/5}. \quad (9)$$

They represent the total mass, the reduced mass, the symmetric mass ratio and the chirp mass, respectively. The rate at which the frequency changes due to the emission of gravitational radiation is given by [17, 27, 31]

$$\begin{aligned} \frac{df}{dt} = \frac{96}{5} \pi^{8/3} \mathcal{M}^{5/3} f^{11/3} & \left[ 1 + \frac{157}{24} I_e f^{-19/9} + \frac{5}{48} \mathcal{S}^2 \bar{\omega} x^{-1} + \frac{96}{5} \beta_g \eta^{2/5} x - \left( \frac{743}{336} + \frac{11}{4} \eta \right) x \right. \\ & \left. + (4\pi - \beta) x^{3/2} + \left( \frac{34103}{18144} + \frac{13661}{2016} \eta + \frac{59}{18} \eta^2 + \sigma \right) x^2 \right], \end{aligned} \quad (10)$$

where we defined the squared internal source velocity,  $x \equiv v^2 = (\pi M f)^{2/3}$ . The first term in the square brackets represents the lowest order quadrupole approximation of general relativity. The second term is the contribution from small eccentricity [32].  $I_e \equiv e_0^2 f_0^{19/9}$  is the asymptotic eccentricity invariant.  $f_0$  is an arbitrary frequency and  $e_0$  is the eccentricity when the frequency of quadrupole gravitational waves is  $f_0$ .  $I_e$  is constant up to the leading order in  $e$ . The third term represents the dipole gravitational radiation in Brans-Dicke theory [14, 15].  $\bar{\omega} \equiv \omega_{\text{BD}}^{-1}$  is the inverse of the Brans-Dicke parameter.  $\mathcal{S} \equiv s_2 - s_1$  with

$$s_i \equiv \left( \frac{\partial(\ln m_i)}{\partial(\ln G_{\text{eff}})} \right)_0, \quad (11)$$

which is called the *sensitivity* of the  $i$ -th body. Here,  $G_{\text{eff}}$  is the gravitational constant at the location of the body and is proportional to the inverse of the Brans-Dicke scalar field there. The subscript 0 denotes that we evaluate  $s_i$  at infinity. This sensitivity roughly equals to the binding energy of the body per unit mass. For example, the sensitivities of white dwarfs and neutron stars are  $s_{\text{WD}} \sim 10^{-3}$  and  $s_{\text{NS}} \sim 0.2$ , respectively. Because of No Hair Theorem, black holes cannot have scalar charges and  $s_{\text{BH}} = 0.5$ . From Eq. (10), the contribution of dipole radiation becomes large as  $\mathcal{S}$  increases. Binaries with large  $\mathcal{S}$  are the ones composed of bodies of different types.

The fourth term is the contribution from the mass of graviton [18]. When graviton is massive, the propagation speed is slower than the speed of light, which modifies the gravitational wave phase from general relativity.  $\beta_g$  is given by [17, 18]

$$\beta_g \equiv \frac{\pi^2 D \mathcal{M}}{\lambda_g^2 (1+z)}, \quad (12)$$

where  $z$  is the cosmological redshift and  $\lambda_g$  is the graviton Compton wavelength. For a flat Universe ( $\Omega_\kappa=0$ ,  $\Omega_\Lambda + \Omega_M = 1$ ), the distance  $D$  is defined as

$$D \equiv \frac{1+z}{H_0} \int_0^z \frac{dz'}{(1+z')^2 \sqrt{\Omega_M(1+z')^3 + \Omega_\Lambda}}. \quad (13)$$

$H_0 = 72 \text{ km/s/Mpc}$  is the Hubble constant, and  $\Omega_M = 0.3$  and  $\Omega_\Lambda = 0.7$  represent density parameters of matter and dark energy, respectively.

The remaining terms are the usual higher order PN terms in general relativity. The quantities  $\beta$  and  $\sigma$  represent spin-orbit and spin-spin contributions to the phase, respectively, given by

$$\beta \equiv \frac{1}{12} \sum_{i=1}^2 \chi_i \left( 113 \frac{m_i^2}{M^2} + 75\eta \right) \hat{\mathbf{L}} \cdot \hat{\mathbf{S}}_i, \quad (14)$$

$$\sigma \equiv \frac{\eta}{48} \chi_1 \chi_2 (-247 \hat{\mathbf{S}}_1 \cdot \hat{\mathbf{S}}_2 + 721 (\hat{\mathbf{L}} \cdot \hat{\mathbf{S}}_1) (\hat{\mathbf{L}} \cdot \hat{\mathbf{S}}_2)), \quad (15)$$

where  $\hat{\mathbf{S}}_i (i = 1, 2)$  are unit vectors in the direction of the spin angular momenta. The spin angular momenta are given by  $\mathbf{S}_i = \chi_i m_i^2 \hat{\mathbf{S}}_i$  where  $\chi_i$  are the dimensionless spin parameters. For black holes, they must be smaller than unity, and for neutron stars, they are generally much smaller than unity. It follows that  $|\beta| \lesssim 9.4$  and  $|\sigma| \lesssim 2.5$  [17].

From  $d\phi/dt = 2\pi f$ , we get the following time and phase evolution of the gravitational radiation by integrating Eq. (10) with time,

$$t(f) = t_c - \frac{5}{256} \mathcal{M} (\pi \mathcal{M} f)^{-8/3} \left[ 1 - \frac{157}{43} I_e f^{-19/9} - \frac{\mathcal{S}^2}{12} \bar{\omega} x^{-1} - \frac{4}{3} \beta_g \eta^{2/5} x + \frac{4}{3} \left( \frac{743}{336} + \frac{11}{4} \eta \right) x \right. \\ \left. - \frac{8}{5} (4\pi - \beta) x^{3/2} + 2 \left( \frac{3058673}{1016064} + \frac{5429}{1008} \eta + \frac{617}{144} \eta^2 - \sigma \right) x^2 \right], \quad (16)$$

$$\phi(f) = \phi_c - \frac{1}{16} (\pi \mathcal{M} f)^{-5/3} \left[ 1 - \frac{785}{344} I_e f^{-19/9} - \frac{25}{336} \mathcal{S}^2 \bar{\omega} x^{-1} - \frac{128}{3} \beta_g \eta^{2/5} x + \frac{5}{3} \left( \frac{743}{336} + \frac{11}{4} \eta \right) x \right. \\ \left. - \frac{5}{2} (4\pi - \beta) x^{3/2} + 5 \left( \frac{3058673}{1016064} + \frac{5429}{1008} \eta + \frac{617}{144} \eta^2 - \sigma \right) x^2 \right], \quad (17)$$

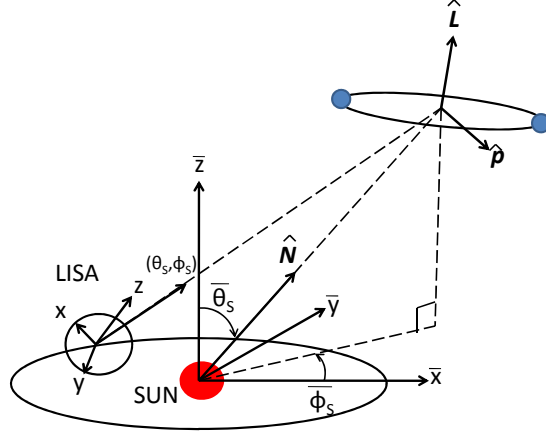


Figure 1: We use two types of coordinates; (i) a barred barycentric frame  $(\bar{x}, \bar{y}, \bar{z})$  tied to the ecliptic and centred in the solar system barycentre; (ii) an unbarred detector frame  $(x, y, z)$ , centred in the barycentre of the triangle and attached to the detector.

where  $t_c$  and  $\phi_c$  are the time and phase at coalescence.

### 3 DETECTOR RESPONSE

LISA is an all-sky monitor with a quadrupolar antenna pattern and consists of three drag-free spacecrafts arranged in an equilateral triangle,  $5 \times 10^6$  km apart. Each spacecraft contains a free-falling mirror so that LISA forms three-arm interferometers with opening angles  $60^\circ$ . The barycentre of each triangle orbits the sun  $20^\circ$  behind the Earth and the detector plane is tilted by  $60^\circ$  with respect to the ecliptic.

Following Cutler [33], we introduce two Cartesian reference frames: (i) a barred barycentric frame  $(\bar{x}, \bar{y}, \bar{z})$  tied to the ecliptic and centred in the solar system barycentre, with  $\hat{\bar{z}}$  normal to the ecliptic and  $\bar{x}\bar{y}$ -plane aligned with the ecliptic; (ii) an unbarred detector frame  $(x, y, z)$ , centred in the barycentre of the triangle and attached to the detector, with  $\hat{z}$  normal to the detector plane (see Fig. 1). The orbit of the detector barycentre can be written as

$$\bar{\theta}(t) = \pi/2, \quad \bar{\phi}(t) = 2\pi t/T, \quad (18)$$

where  $T = 1\text{year}$  and we have assumed  $\bar{\phi}(t=0) = 0$ .

The detector having three arms corresponds to having two individual interferometers. The waveforms measured by each detector are given as

$$h_\alpha(t) = \frac{\sqrt{3}}{2} \frac{2m_1 m_2}{r D_L} A_{\text{pol},\alpha}(t) \cos[\phi(t) + \varphi_{\text{pol},\alpha}(t) + \varphi_D(t)], \quad (19)$$

where  $\alpha = \text{I, II}$  labels the detector number (see Appendix B for more details). The polarisation amplitude  $A_{\text{pol},\alpha}(t)$ , the polarisation phases  $\varphi_{\text{pol},\alpha}(t)$  and the Doppler phase  $\varphi_D(t)$  are defined as follows,

$$A_{\text{pol},\alpha}(t) = \sqrt{(1 + (\hat{\mathbf{L}} \cdot \hat{\mathbf{N}})^2)^2 F_\alpha^+(t)^2 + 4(\hat{\mathbf{L}} \cdot \hat{\mathbf{N}})^2 F_\alpha^\times(t)^2}, \quad (20)$$

$$\cos(\varphi_{\text{pol},\alpha}(t)) = \frac{(1 + (\hat{\mathbf{L}} \cdot \hat{\mathbf{N}})^2) F_\alpha^+(t)}{A_{\text{pol},\alpha}(t)}, \quad (21)$$

$$\sin(\varphi_{\text{pol},\alpha}(t)) = \frac{2(\hat{\mathbf{L}} \cdot \hat{\mathbf{N}}) F_\alpha^\times(t)}{A_{\text{pol},\alpha}(t)}, \quad (22)$$

$$\varphi_D(t) = 2\pi f(t) R \sin \bar{\theta}_S \cos[\bar{\phi}(t) - \bar{\phi}_S], \quad (23)$$

where  $\hat{\mathbf{L}}$  is the unit vector parallel to the orbital angular momentum and  $\hat{\mathbf{N}}$  is the unit vector pointing toward the centre of mass of the binary,  $F_\alpha^+$  and  $F_\alpha^\times$  are the beam-pattern functions of + and  $\times$  polarisation modes for each detectors, shown in the Appendix B.  $(\bar{\theta}_S, \bar{\phi}_S)$  represents the direction of the source in the solar barycentre frame and  $R$  represents 1AU. The Doppler phase denotes the difference between the phase of the wavefront at the detector and the phase of the wavefront at the solar system barycentre. It arises from the motion of the detector around the sun.

Later, we estimate the accuracy of determination of the binary parameters using the matched filtering analysis, where we work on the Fourier domain. Therefore we calculate the Fourier transform of the signal,

$$\tilde{h}_\alpha(f) = \int_{-\infty}^{\infty} dt e^{2\pi i f t} h_\alpha(t). \quad (24)$$

To evaluate this quantity, we use the stationary phase approximation [30]. When conditions  $d \ln A / dt \ll d\phi/dt$  and  $d^2\phi/dt^2 \ll (d\phi/dt)^2$  are satisfied, the saddle point method can be used and the Fourier transform of a function  $B(t) = A(t) \cos \phi(t)$  becomes

$$\tilde{B}(f) \approx \frac{1}{2} A(t) \left( \frac{df}{dt} \right)^{-1/2} \exp i(2\pi f t(f) - \phi(f) - \pi/4). \quad (25)$$

Under this approximation, the Fourier component of the waveform  $\tilde{h}(f)$  becomes [17]

$$\tilde{h}(f) = \frac{\sqrt{3}}{2} \mathcal{A} f^{-6/7} e^{i\Psi(f)} \left[ \frac{5}{4} A_{\text{pol}, \alpha}(t(f)) \right] e^{-i(\varphi_{\text{pol}, \alpha} + \varphi_D)}, \quad (26)$$

where the amplitude  $\mathcal{A}$  and the phase  $\Psi(f)$  are given by

$$\mathcal{A} = \frac{1}{\sqrt{30\pi^{2/3}}} \frac{\mathcal{M}^{5/6}}{D_L}, \quad (27)$$

$$\begin{aligned} \Psi(f) = & 2\pi f t_c - \phi_c - \frac{\pi}{4} + \frac{3}{128} (\pi \mathcal{M} f)^{-5/3} \left[ 1 - \frac{5}{84} \mathcal{S}^2 \bar{\omega} x^{-1} - \frac{128}{3} \beta_g \eta^{2/5} x - \frac{2355}{1462} I_e f^{-19/9} \right. \\ & \left. + \left( \frac{3715}{756} + \frac{55}{9} \eta \right) x - 4(4\pi - \beta) x^{3/2} + \left( \frac{15293365}{508032} + \frac{27145}{504} \eta + \frac{3085}{72} \eta^2 - 10\sigma \right) x^2 \right]. \end{aligned} \quad (28)$$

Also, when we integrate out the angle-dependence from the waveform (26), it becomes

$$\tilde{h}(f) = \frac{\sqrt{3}}{2} \mathcal{A} f^{-6/7} e^{i\Psi(f)}. \quad (29)$$

## 4 PRECESSION

In this section, we introduce an additional effect, the precession. The spin-orbit interaction and spin-spin interaction change the orientations of the orbital angular momentum vector  $\mathbf{L}$  and the spin vectors  $\mathbf{S}_i$ . These vectors precess over a timescale longer than the orbital period but shorter than the observation timescale. This effect drastically changes the detected waveforms.

### 4.1 Simple Precession

In this paper, we assume that one of the spins of the binary objects is negligible (i.e.  $\mathbf{S}_1 \sim 0$ ). We also assume that the orbital angular momentum  $\mathbf{L}$  is neither parallel nor antiparallel to the total spin angular momentum  $\mathbf{S}(= \mathbf{S}_1 + \mathbf{S}_2)$ . Then, the precession equations become

$$\dot{L} = -\frac{32\mu^2}{5r} \left(\frac{M}{r}\right)^{5/2}, \quad (30)$$

$$\dot{S} = 0, \quad (31)$$

$$\dot{\hat{L}} = \left(2 + \frac{3m_2}{2m_1}\right) \frac{\mathbf{J}}{r^3} \times \hat{L}, \quad (32)$$

$$\dot{\hat{S}} = \left(2 + \frac{3m_2}{2m_1}\right) \frac{\mathbf{J}}{r^3} \times \hat{S}, \quad (33)$$

where  $\mathbf{J}$  is the total angular momentum  $\mathbf{J} \equiv \mathbf{L} + \mathbf{S}$ . Under this simple precession, the following quantities become constant during the inspiral;  $\mathbf{S}_1 \cdot \mathbf{S}_2$ ,  $\kappa \equiv \hat{\mathbf{L}} \cdot \hat{\mathbf{S}}$ , and the magnitude of the total spin angular momentum  $S \equiv |\mathbf{S}_1 + \mathbf{S}_2|$ . From the above equations, it can be seen that both  $\hat{\mathbf{L}}$  and  $\hat{\mathbf{S}}$  precess around  $\mathbf{J}$  with angular velocity

$$\Omega_p = \left(2 + \frac{3m_2}{2m_1}\right) \frac{J}{r^3}. \quad (34)$$

In general, the precessing timescale  $\Omega_p^{-1}$  is shorter than the inspiral timescale  $L/|\dot{L}|$ . Therefore from  $\dot{\mathbf{J}} = \dot{\mathbf{L}}$ ,  $\mathbf{J}$  changes in magnitude but the direction is almost constant. Then, the analytic form of  $\hat{\mathbf{L}}$  can be obtained up to some approximate orders (see Appendix C).

## 4.2 Detector Response

When precession is taken into account, the principal axis  $\hat{\mathbf{N}} \times \hat{\mathbf{L}}$  varies with time so that the GW phase evolution  $\phi(t)$  no longer equals to twice the orbital phase  $\phi_{\text{orb}}(t) \equiv \int \Omega(t) dt$ . We define this difference  $2\delta\phi(t)$  by

$$\phi(t) = 2\phi_{\text{orb}}(t) + 2\delta\phi(t). \quad (35)$$

This  $\delta\phi(t)$  is the so-called *Thomas precession phase*. We specify the constant of integration so that  $\phi_{\text{orb}}(t_c) = \phi_c$ . In general,  $\delta\phi(t_c) \neq 0$  so that  $\phi_c$  does not equal to  $\phi(t_c)$  anymore in this case. From Eqs. (85) and (35), the detector output  $h_\alpha(t)$  becomes

$$\begin{aligned} h_\alpha(t) &= \frac{\sqrt{3}}{2} A_+ F_\alpha^+(\theta_S, \phi_S, \psi_S) \cos 2(\phi_{\text{orb}}(t) + \delta\phi(t)) + \frac{\sqrt{3}}{2} A_\times F_\alpha^\times(\theta_S, \phi_S, \psi_S) \sin 2(\phi_{\text{orb}}(t) + \delta\phi(t)) \\ &= \frac{2m_1 m_2}{rD} (F_\alpha^{\cos} \cos 2\phi_{\text{orb}} + F_\alpha^{\sin} \sin 2\phi_{\text{orb}}), \end{aligned} \quad (36)$$

where  $\alpha = \text{I, II}$  labels the detector number and  $F_\alpha^{\cos}$  and  $F_\alpha^{\sin}$  are defined as follows;

$$F_\alpha^{\cos} \equiv (1 + (\hat{\mathbf{L}} \cdot \hat{\mathbf{N}})^2) F_\alpha^+ \cos 2\delta\phi - 2(\hat{\mathbf{L}} \cdot \hat{\mathbf{N}}) F_\alpha^\times \sin 2\delta\phi, \quad (37)$$

$$F_\alpha^{\sin} \equiv -(1 + (\hat{\mathbf{L}} \cdot \hat{\mathbf{N}})^2) F_\alpha^+ \sin 2\delta\phi - 2(\hat{\mathbf{L}} \cdot \hat{\mathbf{N}}) F_\alpha^\times \cos 2\delta\phi. \quad (38)$$

Following Eq. (19), we express this output (36) in terms of an amplitude and phase form, and we also take the motions of the detectors into account to obtain

$$h_\alpha(t) = \frac{2m_1 m_2}{rD} A_{\text{pol},\alpha}^{\text{prec}}(t) \cos(2\phi_{\text{orb}}(t) + \varphi_{\text{pol},\alpha}^{\text{prec}}(t) + \varphi_D(t)), \quad (39)$$

where  $A_{\text{pol},\alpha}^{\text{prec}}(t)$  and  $\varphi_{\text{pol},\alpha}^{\text{prec}}(t)$  are given as



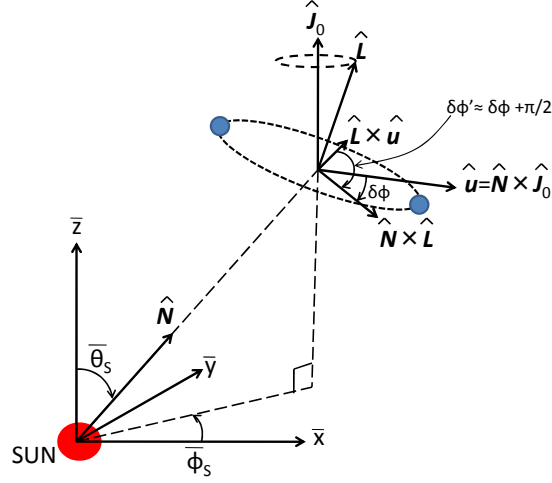


Figure 2: The Thomas precession phase  $\delta\phi(t)$  is the angle from the vector  $\hat{\mathbf{u}}$  to the principal axis  $\hat{\mathbf{N}} \times \hat{\mathbf{L}}$ . We define  $\delta\phi'$  as the angle from the vector  $\hat{\mathbf{L}} \times \hat{\mathbf{u}}$  to the one  $\hat{\mathbf{N}} \times \hat{\mathbf{L}}$ . Notice that these two vectors always lie on the orbital plane.  $\delta\phi'$  equals to  $\delta\phi + \pi/2$  up to  $O(|\delta\mathbf{L}|/L)$ .

$$A_{\text{pol},\alpha}^{\text{prec}}(t) = \sqrt{(F_{\alpha}^{\cos}(t))^2 + (F_{\alpha}^{\sin}(t))^2}, \quad (40)$$

$$\cos(\varphi_{\text{pol},\alpha}^{\text{prec}}(t)) = \frac{F_{\alpha}^{\cos}(t)}{A_{\text{pol},\alpha}^{\text{prec}}(t)}, \quad (41)$$

$$\sin(\varphi_{\text{pol},\alpha}^{\text{prec}}(t)) = -\frac{F_{\alpha}^{\sin}(t)}{A_{\text{pol},\alpha}^{\text{prec}}(t)}. \quad (42)$$

The quantities  $(\hat{\mathbf{L}} \cdot \hat{\mathbf{N}}), (\hat{\mathbf{L}} \cdot \hat{\mathbf{z}})$  and  $[\hat{\mathbf{N}} \cdot (\hat{\mathbf{L}} \times \hat{\mathbf{z}})]$ , which are needed to compute the polarisation angle  $\psi_S(t)$  in the beam pattern coefficients  $F_{\alpha}^{+}$  and  $F_{\alpha}^{\times}$ , are expressed in the Appendix C.

Finally, we need to calculate the Thomas precession phase  $\delta\phi(t)$ . Apostolatos *et al.* [26] derived the explicit form as

$$\delta\phi(t) = - \int_t^{t_c} dt \left( \frac{\hat{\mathbf{L}} \cdot \hat{\mathbf{N}}}{1 - (\hat{\mathbf{L}} \cdot \hat{\mathbf{N}})^2} \right) (\hat{\mathbf{L}} \times \hat{\mathbf{N}}) \cdot \dot{\hat{\mathbf{L}}}. \quad (43)$$

This expression includes an integration which makes the computational time very long. Vecchio [20] estimated the binary parameter accuracies by choosing a few random sources with and without including  $\delta\phi(t)$  and found that this term did not affect the results, and concluded that this term could be neglected. This is true for the binaries for which  $\hat{\mathbf{L}} \cdot \hat{\mathbf{N}}$  never becomes close to  $\pm 1$ . However, when  $\hat{\mathbf{L}} \cdot \hat{\mathbf{N}} \approx \pm 1$ , the principal axis changes rapidly with time. This also makes the polarisation angle  $\psi_S(t)$  changes rapidly. Since it is the Thomas precession phase  $\delta\phi(t)$  that cancels this rapid change, this cannot be neglected in this case.

The direction which  $\delta\phi$  is measured from is arbitrary. It can be seen from Eq. (43) that Apostolatos *et al.* [26] defined  $\delta\phi$  as the angle from the principal axis at the time of coalescence  $(\hat{\mathbf{N}} \times \hat{\mathbf{L}})_{t=t_c}$  to the one  $(\hat{\mathbf{N}} \times \hat{\mathbf{L}})_t$  at a time  $t$ . In general, since  $(\hat{\mathbf{N}} \times \hat{\mathbf{L}})_{t=t_c}$  does not lie on the orbital plane at a time  $t$ , we need to follow the evolution of the principal axis to calculate the Thomas precession  $\delta\phi(t)$ . This is the reason why the integration appears in Eq. (43).

Here, we try to derive the approximate expression of  $\delta\phi(t)$  that is not in the integral form. To do so, we use a specific vector  $\hat{\mathbf{L}} \times \hat{\mathbf{u}}$  that always lie on the orbital plane, where  $\hat{\mathbf{u}}$  is a constant unit vector. In

the limit of a large separation (i.e.  $t \rightarrow -\infty$  or  $L \rightarrow \infty$ ),  $\hat{\mathbf{L}}$  approaches to  $\hat{\mathbf{J}}_0$ . Using this  $\hat{\mathbf{J}}_0$ , we take  $\hat{\mathbf{u}} = \hat{\mathbf{N}} \times \hat{\mathbf{J}}_0$  (see Fig. 2). We define an approximate Thomas precession phase  $\delta\phi(t)$  as the angle from this vector  $\hat{\mathbf{u}}$  to the principal axis  $\hat{\mathbf{N}} \times \hat{\mathbf{L}}$ . (We may take the vector  $\hat{\mathbf{u}}$  to be the principal axis at the time of coalescence  $(\hat{\mathbf{N}} \times \hat{\mathbf{L}})_{t=t_c}$ . Then,  $\delta\phi(t_c)$  becomes 0 and  $\phi(t_c) = \phi_c$ . However, the computation is easier for choosing  $\hat{\mathbf{u}}$  to be  $\hat{\mathbf{N}} \times \hat{\mathbf{J}}_0$ .) We denote the angle from  $\hat{\mathbf{L}} \times \hat{\mathbf{u}}$  to  $\hat{\mathbf{N}} \times \hat{\mathbf{L}}$  as  $\delta\phi'$ , and the difference between  $\mathbf{J}_0$  and  $\mathbf{L}$  as  $\delta\mathbf{L}$ ;  $\mathbf{L} = \mathbf{J}_0 + \delta\mathbf{L}$ . Then,  $\delta\phi'$  can be related to  $\delta\phi$  as  $\delta\phi' = \delta\phi + \pi/2$  up to  $O(|\delta\mathbf{L}|/L)$ . As  $\delta\phi'$  always lie on the orbital plane, by using this angle we can express  $\delta\phi(t)$  without integration.  $\sin\delta\phi$  and  $\cos\delta\phi$  can be written as

$$\sin\delta\phi = -\cos\delta\phi' = -\frac{(\hat{\mathbf{L}} \times \hat{\mathbf{N}}) \cdot (\hat{\mathbf{L}} \times \hat{\mathbf{u}})}{|\hat{\mathbf{L}} \times \hat{\mathbf{N}}||\hat{\mathbf{L}} \times \hat{\mathbf{u}}|} \quad (44)$$

$$= \frac{(\hat{\mathbf{L}} \cdot \hat{\mathbf{N}})(\hat{\mathbf{L}} \cdot \hat{\mathbf{u}})}{\sqrt{(1 - (\hat{\mathbf{L}} \cdot \hat{\mathbf{N}})^2)(1 - (\hat{\mathbf{L}} \cdot \hat{\mathbf{u}})^2)}},$$

$$\cos\delta\phi = \sin\delta\phi' = -\frac{\hat{\mathbf{N}} \cdot (\hat{\mathbf{L}} \times \hat{\mathbf{u}})}{\sqrt{(1 - (\hat{\mathbf{L}} \cdot \hat{\mathbf{N}})^2)(1 - (\hat{\mathbf{L}} \cdot \hat{\mathbf{u}})^2)}}. \quad (45)$$

Therefore the Thomas precession phase  $\delta\phi(t)$  can be expressed as

$$\delta\phi = \arctan\left(-\frac{(\hat{\mathbf{L}} \cdot \hat{\mathbf{N}})(\hat{\mathbf{L}} \cdot \hat{\mathbf{u}})}{\hat{\mathbf{N}} \cdot (\hat{\mathbf{L}} \times \hat{\mathbf{u}})}\right). \quad (46)$$

## 5 PARAMETER ESTIMATION

We use the matched filtering analysis to estimate the determination errors of the binary parameters  $\boldsymbol{\theta}$  [34, 30]. We assume that the detector noise is stationary and Gaussian. ‘‘Stationarity’’ means that the different Fourier components  $\tilde{n}(f)$  of the noise are uncorrelated and we have

$$\langle \tilde{n}^*(f) \tilde{n}(f') \rangle = \delta(f - f') \frac{1}{2} S_n(f). \quad (47)$$

Here,  $\langle \dots \rangle$  denotes the expectation value and  $S_n(f)$  is the noise spectral density. It can be seen that the noise r.m.s. is proportional to  $\frac{1}{2} S_n(f)$ . Therefore the Gaussian probability distribution of the noise is

$$p(n_0) \propto \exp\left[-\frac{1}{2} \int_{-\infty}^{\infty} df \frac{|\tilde{n}_0(f)|^2}{(1/2)S_n(f)}\right]$$

$$\propto \exp\left[-\frac{1}{2}(n_0|n_0)\right], \quad (48)$$

where we have defined the inner product as

$$(A|B) = \text{Re} \int_{-\infty}^{\infty} df \frac{\tilde{A}^*(f) \tilde{B}(f)}{\frac{1}{2} S_n(f)}$$

$$= 4 \text{Re} \int_0^{\infty} df \frac{\tilde{A}^*(f) \tilde{B}(f)}{S_n(f)}. \quad (49)$$

The signal to noise ratio(SNR) for a given  $h$  is

$$\rho[h] \equiv \sqrt{(h|h)}. \quad (50)$$

The detected signal  $s(t)$  is the sum of the gravitational wave signal  $h(t; \boldsymbol{\theta})$  and the noise  $n(t)$ ;  $s(t) = h(t, \boldsymbol{\theta}_t) + n_0(t)$  where  $\boldsymbol{\theta}_t$  is the true binary parameters and  $n_0(t)$  is the noise of this specific measurement. Then, Eq. (48) becomes

$$p(\theta_t|s) \propto p^{(0)}(\theta_t) \exp \left[ (h_t|s) - \frac{1}{2}(h_t|h_t) \right], \quad (51)$$

where  $p^{(0)}(\theta_t)$  represents the distribution of prior information and  $h_t \equiv h(\theta_t)$ . We determine the binary parameters as  $\hat{\theta}$  that maximise the probability distribution  $p(\theta_t|s)$ . Then  $\hat{\theta}$  is the solution of the following equation;

$$(\partial_i h_t|s) - (\partial_i h_t|h_t) = 0. \quad (52)$$

where  $\frac{\partial}{\partial \theta_i} = \partial_i$ . We denote an estimate of the r.m.s. error as  $\Delta\theta^i$ ;  $\theta^i = \hat{\theta}^i + \Delta\theta^i$ . Next, we expand Eq. (51) in powers of  $\Delta\theta^i$  up to quadratic order and we get

$$p(\theta|s) \propto p^{(0)}(\theta) \exp \left[ -\frac{1}{2} \Gamma_{ij} \Delta\theta^i \Delta\theta^j \right], \quad (53)$$

where  $\Gamma_{ij} = (\partial_i \partial_j h|h - s) + (\partial_i h|\partial_j h)$  is called Fisher matrix. Since  $h - s = -n$ , in the limit of large SNR, we can neglect the first term of  $\Gamma_{ij}$  and

$$\Gamma_{ij} = (\partial_i h|\partial_j h). \quad (54)$$

Then, r.m.s. of  $\Delta\theta^i$  can be calculated by taking the square root of the diagonal elements of the covariance matrix  $\Sigma^{ij}$ , which is the inverse of the Fisher matrix;

$$\langle \Delta\theta^i \Delta\theta^j \rangle = \Sigma^{ij}, \quad \Sigma^{ij} \equiv (\Gamma^{-1})^{ij}. \quad (55)$$

We take into account our prior information on the maximum spin by assuming

$$p^{(0)}(\theta) \propto \exp \left[ -\frac{1}{2} \left( \frac{\beta}{9.4} \right)^2 - \frac{1}{2} \left( \frac{\sigma}{2.5} \right)^2 \right]. \quad (56)$$

## 6 LISA NOISE SPECTRUM

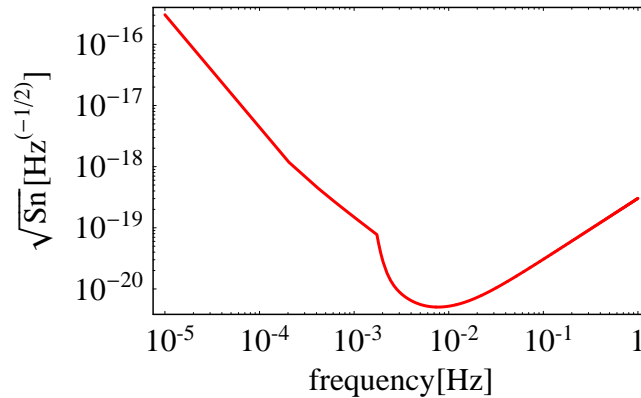


Figure 3: The noise spectral density for LISA.

In this section, we introduce the noise spectrum of LISA following Ref. [29]. The instrumental noise spectral density for LISA is given as

$$S_h^{\text{inst}}(f) = \left[ 9.18 \times 10^{-52} \left( \frac{f}{1 \text{ Hz}} \right)^{-4} + 1.59 \times 10^{-41} + 9.18 \times 10^{-38} \left( \frac{f}{1 \text{ Hz}} \right)^2 \right] \text{ Hz}^{-1}. \quad (57)$$

Besides instrumental noise, there are foreground confusion noises. These confusion noise spectral densities and the energy densities of gravitational waves are related as follows;

$$S_h^{\text{conf}} = \frac{3}{5\pi} f^{-3} \rho_c \Omega_{\text{GW}}, \quad (58)$$

where  $\rho_c \equiv \frac{3H_0^2}{8\pi}$  is the critical energy density of the universe and

$$\Omega_{\text{GW}} \equiv \frac{1}{\rho_c} \frac{d\rho_{\text{GW}}}{d \ln f} \quad (59)$$

is the energy density of gravitational waves per log frequency normalised by  $\rho_c$ . The energy density of gravitational waves coming from extra-galactic white dwarf binaries has been estimated as  $\Omega_{\text{GW}} = 3.6 \times 10^{-12} (f/10^{-3} \text{Hz})^{2/3}$  and the noise spectral density becomes [35]

$$S_h^{\text{ex-gal}}(f) = 4.2 \times 10^{-47} \left( \frac{f}{1 \text{ Hz}} \right)^{-7/3} \text{Hz}^{-1}. \quad (60)$$

On the other hand, the energy density of gravitational waves coming from galactic white dwarf binaries has been calculated as 50 times larger than the one coming from extra-galactic white dwarf binaries. Therefore the noise spectral density becomes [36]

$$S_h^{\text{gal}}(f) = 2.1 \times 10^{-45} \left( \frac{f}{1 \text{ Hz}} \right)^{-7/3} \text{Hz}^{-1}. \quad (61)$$

We compute the total noise spectral density as

$$S_h(f) = \min \left[ \frac{S_h^{\text{inst}}(f)}{\exp(-\kappa T^{-1} dN/df)}, S_h^{\text{inst}}(f) + S_h^{\text{gal}}(f) \right] + S_h^{\text{ex-gal}}(f). \quad (62)$$

Here  $dN/df$  is the number density of galactic white dwarf binaries per unit frequency, for which we use the estimate [37]

$$\frac{dN}{df} = 2 \times 10^{-3} \text{Hz}^{-1} \left( \frac{f}{1 \text{ Hz}} \right)^{-11/3}. \quad (63)$$

$\kappa \simeq 4.5$  is the average number of frequency bins that are lost when each galactic binary is fitted out. This noise curve is drawn in Fig. 3

## 7 NUMERICAL CALCULATIONS AND RESULTS

Following Berti *et al.* [17], we estimate how accurately we can determine binary parameters by detecting inspiral gravitational waves with LISA. The total noise spectral density for LISA is given by Eq. (62) and we introduce the cutoff frequencies for LISA as follows;

$$f_{\text{low}} = 10^{-5} \text{Hz}, \quad f_{\text{high}} = 1 \text{Hz}. \quad (64)$$

Here, we use the matched filtering analysis, assuming that the observation starts 1 year before the coalescence. We assume that we use two detectors. We numerically calculate the determination error of each parameter which is given by the square root of the inverse of the Fisher matrix  $\Gamma_{ij}$ . We use the Gauss-Jordan elimination [38] for inverting the Fisher matrix. In calculating this  $\Gamma_{ij}$ , we need to perform the integration in the frequency domain. Following Ref. [17], we take the frequency range of this integration as  $(f_{\text{in}}, f_{\text{fin}})$ ;

$$f_{\text{in}} = \max\{f_{\text{low}}, f_{1\text{yr}}\}, \quad f_{\text{fin}} = \min\{f_{\text{high}}, f_{\text{ISCO}}\}, \quad (65)$$

where

$$f_{1\text{yr}} = 4.149 \times 10^{-5} \left[ \left( \frac{\mathcal{M}}{10^6 M_\odot} \right)^{-5/8} \left( \frac{T_{\text{obs}}}{1\text{yr}} \right)^{-3/8} \right] \quad (66)$$

is the frequency 1year before the coalescence, and  $f_{\text{ISCO}}$  is given as

$$f_{\text{ISCO}} = \frac{1}{6^{3/2}\pi M_{\text{BH}}}. \quad (67)$$

For the waveforms, we use the *restricted 2PN waveforms*. We only take up to 2PN because spin terms are known only to this order. There are 15 parameters in total; the chirp mass  $\ln \mathcal{M}$ , the dimensionless mass parameter  $\ln \eta$ ; the coalescence time  $t_c$ , the coalescence phase  $\phi_c$ ; the distance to the source  $\ln D$ ; the spin-orbit coupling coefficient  $\beta$ , the spin-spin coupling coefficient  $\sigma$ ; the inner product of the orbital angular momentum and the spin angular momentum  $\kappa$ , the precession angle  $\alpha_c$  that characterises  $\alpha$  at the time of coalescence (the precession angle  $\alpha$  is defined in Appendix C); the squared eccentricity  $e_0^2$  at the specific frequency  $f_0$ ;  $(\theta_S, \phi_S)$  for the initial direction of the source,  $(\theta_J, \phi_J)$  for the initial direction of the total angular momentum; finally,  $\bar{\omega}$ , the inverse of the Brans-Dicke parameter, or  $\beta_g$ , the quantity that is proportional to the square inverse of the graviton Compton wavelength  $\lambda_g$ , depending on which theory we are aiming to constrain. For constraining the Brans-Dicke parameter, we consider NS/IMBH binaries, assuming the difference between NS and BH sensitivities to be  $\mathcal{S} = 0.3$ . For constraining the graviton mass, we consider SMBH/BH binaries at 3Gpc. In this case, we fix the cosmological parameters as follows;  $\Omega_\kappa = \Omega_{\text{rad}} = 0$ ,  $\Omega_m = 0.3$ ,  $\Omega_\Lambda = 0.7$ . We also fix the Hubble constant as  $H_0 = 72$  km/s/Mpc. There are three main differences from Ref. [17].

(i) We include the spin-spin interaction  $\sigma$ : Berti et al. [17] reported that when they included both  $\sigma$  and the parameter for the alternative theories of gravity like  $\bar{\omega}$ , the ratio (we denote this by  $R$ ) between the smallest to the largest eigen value of the Fisher matrix  $\mathbf{\Gamma}$  approached their machine's floating-point precision, and they could not obtain enough accuracy for the inversion of this matrix. We overcome this difficulty by performing our numerical calculations in quadruple precisions. Also, we use the trick explained in the appendix D to make sure the numerical inversion is correctly performed. Basically, we rescale the basis vector so as to make all the diagonal components of the Fisher matrix equal to 1, then take the inverse of this normalised matrix, and finally put the factor for the rescaling back to obtain the inverse of our original Fisher matrix. Even if the ratio  $R$  approaches the machine's floating point precision, the one of the normalised Fisher matrix can be smaller than the floating point so that the inversion can be performed correctly.

(ii) We take the small eccentricity into account: The binary system gradually loses energy and angular momentum because of the gravitational radiation which circularises the orbit. In fact, since the eccentricity decreases according to  $e \propto f^{-19/18}$  [19], usually one assumes that the eccentricity is known to be 0 a priori and does not include this into binary parameters. Still, we should take this into account for more practical analysis since we cannot set the eccentricity to 0 a priori. The values that we take for  $e_0$  is explained in the appendix.

(iii) We also take the spin precession into account: In this case, the orbital angular momentum  $\mathbf{L}$  oscillates, which introduces the additional oscillations in both the amplitude and the phase of the waveform. This additional information solves degeneracy in the binary parameters, enhancing the determination accuracy. The parameter estimation including precession has been estimated by several authors using LISA [20, 21] and using the detectors on the ground [22, 23, 24, 25], in the framework of general relativity. Our calculation is the first one to include precession in parameter estimation in the context of modified gravity.. We consider the simple precession by assuming that one of the spins of the binary objects is 0. References [20, 22, 23, 24, 25] estimated the determination errors of the binary parameters under this simple precession.

## 7.1 No precession

In this subsection, we show the results without spin precession. In this case,  $\kappa$  and  $\alpha_c$  are excluded from our binary parameters. Following Ref. [17], we perform the numerical integration using the Gauss-Legendre routine GAULEG [38]. Gauss-Legendre quadrature takes the abscissas at the zeros of the  $N$ -th Legendre polynomials. With this method, integrand polynomials up to  $(2N - 1)$ -th order can be calculated exactly. We take the number of frequency bins to be 600. The nominal values of the parameters are  $t_c = \phi_c = \beta = \sigma = \bar{\omega} = \beta_g = 0$ . We change the masses of the binary objects and calculate the eccentricity  $e_0$  for each case (see Appendix A). The frequency  $f_0$  at which the eccentricity takes

Table 1: The results of error estimation in Brans-Dicke theory. These are calculated with pattern-averaged analysis for NS/BH binaries with masses  $(1.4 + 400)M_\odot$ ,  $(1.4 + 400)M_\odot$ ,  $(1.4 + 400)M_\odot$  and  $(1.4 + 400)M_\odot$  for  $\rho = 10$ . For each binary, the first line represents the results shown in [17] which does not include  $\sigma$  nor  $e_0^2$  into parameters. The second line represents the results taking  $\sigma$  into account, and the third line shows the ones that include both  $\sigma$  and  $e_0^2$ . We used only one detector for the analyses.

$\sigma$	$e_0^2$	$\lambda_g(10^{20}\text{cm})$	$\Delta \ln \mathcal{M}(\%)$	$\Delta \ln \eta$	$\Delta \beta$	$\Delta t_c(s)$	$\Delta \phi_c$	$\Delta \sigma$	$\Delta e_0^2(10^{-6})$
$400M_\odot$									
$\times$	$\times$	39190	0.00657	0.0250	0.0508	7.95	76.7	-	-
$\bigcirc$	$\times$	24886	0.0130	0.0819	0.202	13.8	552	2.39	-
$\bigcirc$	$\bigcirc$	4583	0.0396	0.142	0.280	16.7	552	2.49	3.18
$1000M_\odot$									
$\times$	$\times$	21257	0.00764	0.0186	0.0557	7.99	58.4	-	-
$\bigcirc$	$\times$	8210	0.0265	0.110	0.0692	23.5	919	1.96	-
$\bigcirc$	$\bigcirc$	1881	0.0692	0.193	0.261	23.6	1059	2.41	2.68
$5000M_\odot$									
$\times$	$\times$	6486	0.0114	0.0133	0.0550	8.79	23.4	-	-
$\bigcirc$	$\times$	1933	0.0503	0.0936	0.221	37.9	1108	0.595	-
$\bigcirc$	$\bigcirc$	281	0.224	0.302	0.916	62.9	2438	1.30	2.97
$10000M_\odot$									
$\times$	$\times$	3076	0.0178	0.0161	0.0706	13.6	15.5	-	-
$\bigcirc$	$\times$	862	0.0827	0.114	0.350	82.9	1763	0.474	-
$\bigcirc$	$\bigcirc$	113	0.412	0.418	1.51	160	4454	1.11	3.35

the value  $e_0$  is chosen as  $f_0 = 0.3\text{Hz}$  for NS/BH binaries and  $f_0 = 10^{-4}\text{Hz}$  for SMBH/BH binaries. We treat the angles  $(\theta_s, \phi_s)$  and  $(\theta_j, \phi_j)$  in two different ways. First, we take the average of these angles and calculate the determination accuracy of the binary parameters. We call this pattern-averaged estimate and we use only 1 detector for the analysis. The second one is the Monte Carlo simulation. We randomly distribute  $10^4$  binaries ( $10^4$  sets of these angles), calculate the determination accuracy for each binary, and take the average at the end. In this case, we use 2 detectors for the analysis.

### 7.1.1 Pattern-averaged estimates

In the case of pattern-averaged estimates, there are only 9 parameters in total;  $\ln \mathcal{M}, \ln \eta, t_c, \phi_c, D_L, \beta, \sigma, e_0$  and  $\bar{\omega}$  or  $\beta_g$ . The waveform is given by Eq. (29). The derivative of this waveform with respect to each parameter is taken analytically as shown in the appendix E.

#### Brans-Dicke Theory:

Here, we consider the parameter estimation in the context of Brans-Dicke theory. We think of four NS/BH binaries of SNR=10; we fix  $m_{\text{NS}} = 1.4M_\odot$  and take  $m_{\text{BH}} = 400, 1000, 5000$  and  $10^4 M_\odot$ . For each binary, we show three results in Table 1; the first line represents the determination accuracies of binary parameters without taking  $\sigma$  and  $e_0^2$  into parameters (the same estimates by Berti *et al.* [17]); the second line shows the results including  $\sigma$  but not  $e_0^2$  into parameters, and the third line shows the ones including both  $\sigma$  and  $e_0^2$  into parameters.

From this table, one can see that adding parameters reduce the determination accuracy. This is because the parameters are strongly correlated and adding parameters dilute the binary information in the detected gravitational waves. Including both  $\sigma$  and  $e_0^2$  into parameters increases the determination errors by roughly one order of magnitude. Especially, including  $e_0^2$  increases the errors on  $\omega_{\text{BD}}$  more than just including  $\sigma$ . The reason for this is as follows. In the phase  $\Psi(f)$ , the term containing  $\omega_{\text{BD}}$  depends on  $f^{-2/3}$ , whilst the ones containing  $\sigma$  and  $e_0^2$  have the dependence  $f^{4/3}$  and  $f^{-19/9}$  respectively. The terms constraining  $\omega_{\text{BD}}$  and  $e_0^2$  both have the negative and similar power dependence on the frequency. Therefore  $\omega_{\text{BD}}$  has stronger correlation with  $e_0^2$  than  $\sigma$ .

Comparing the constraints from the binaries having different BH mass, one can see that the constraint becomes more stringent as the BH mass decreases. This is because the orbital velocity of the binaries become slower, which makes the dipole contribution relatively greater.

In Fig. 4, we plot the curve of constant probability on the  $\Delta e_0^2$ - $\Delta\bar{\omega}$  plane for  $(1.4 + 400)M_\odot$  NS/BH binary with  $\rho = 10$ . The fiducial values lie at the centre of the ellipse at 68% confidence level. Since  $e_0^2$  is always positive, it can be understood from this figure that we can decrease the upper bound on  $\Delta\bar{\omega}$  by imposing the prior  $e_0^2 > 0$ . In fact, the upper limit for  $\Delta\bar{\omega}$  is obtained at  $\Delta e_0^2 = 0$  in this case. This means that when we include the prior above, the constraint on  $\omega_{\text{BD}}$  including eccentricity should be similar to the case without taking eccentricity into account. Therefore we conclude that the constraint on  $\omega_{\text{BD}}$  is not so much affected by taking eccentricity into account..

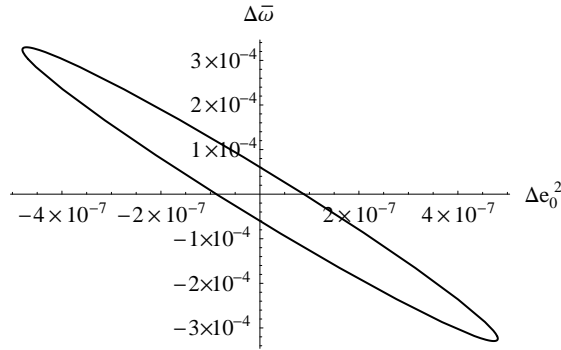


Figure 4: The curve showing constant probability on the  $\Delta e^2$ - $\Delta\bar{\omega}$  plane for  $(1.4 + 400)M_\odot$  NS/BH binary with  $\rho = 10$ , such that the fiducial values lie at the centre of the ellipse at 68% confidence level

### Massive Graviton Theories:

Next, we consider the parameter estimation in the context of massive graviton theories. We also consider four BH/BH binaries in this case;  $(10^7 + 10^7)M_\odot$ ,  $(10^7 + 10^6)M_\odot$ ,  $(10^6 + 10^6)M_\odot$  and  $(10^6 + 10^5)M_\odot$ . As in the Brans-Dicke case, we perform three types of analyses whose results are shown in Table 2. Berti *et al.* [17] reported that the effect of adding prior information on the maximum spin is negligible. However, we found that including prior information changes the results about a few percent. Moreover, Berti *et al.* have claimed that when they include both  $\sigma$  and  $\bar{\omega}$  or  $\beta_g$  into parameters, they cannot take the inverse of the Fisher matrix properly. However, when we include the prior information, the matrix inverse can be performed successfully. We decided to include the prior information, and do the calculations in quadruple precision. This is why the first column of each binaries in Table 2 slightly differs from the results shown in Ref. [17].

From Table 2, it can be seen that in this case, including both  $\sigma$  and  $e_0^2$  into parameters reduces the accuracy only by a factor of a few. This indicates that  $\beta_g$  is only weakly correlated with other parameters. In the massive graviton case, including  $\sigma$  affects the constraint on  $\lambda_g$  more than including  $e_0^2$ . The reason is the same as in the case of Brans-Dicke; since the terms containing  $\lambda_g$  and  $\sigma$  in the phase  $\Psi(f)$  both have the positive power dependence on frequency, their correlation is stronger than the one between  $\lambda_g$  and  $e_0^2$ .

Figure 5 shows the the curve of constant probability on the  $\Delta e_0^2$ - $\Delta\beta_g$  plane for  $(10^7 + 10^7)M_\odot$  SMBH/BH binary at 3Gpc. The fiducial values lie at the centre of the ellipse at 68% confidence level. Compared to Fig. 4 of Brans-Dicke theory, it can be seen that the ellipse is slightly tilted in the other way. This indicates that the constraint on  $\lambda_g$  would not change even if we impose the prior  $\Delta e_0^2 > 0$ . However, this ellipse is tilted only slightly, which suggests that  $\beta_g$  and  $e_0^2$  are correlated only weakly, as we have stated above. Therefore, the constraint on  $\lambda_g$  is affected only weakly by the inclusion of  $e_0^2$  into parameters.

When the graviton has a finite mass, its velocity is expressed as [18]

Table 2: The results of error estimation in massive graviton theories. These are calculated with pattern-averaged analysis for SMBH/BH binaries with masses  $(10^7 + 10^7)M_\odot$ ,  $(10^7 + 10^6)M_\odot$ ,  $(10^6 + 10^6)M_\odot$  and  $(10^6 + 10^5)M_\odot$  at 3Gpc. As in the Brans-Dicke case, the first line of each binary represents the estimation without taking  $\sigma$  nor  $e_0^2$  into parameters. These results do not exactly match with the ones shown in [17] because we also considered prior information. The meaning of second and third lines are the same as in Table 1.

$\sigma$	$e_0^2$	$\lambda_g(10^{20}\text{cm})$	$\Delta \ln \mathcal{M}(\%)$	$\Delta \ln \eta$	$\Delta \beta$	$\Delta t_c(s)$	$\Delta \phi_c$	$\Delta \sigma$	$\Delta e_0^2(10^{-6})$
$(10^7 + 10^7)M_\odot$									
$\times$	$\times$	22.77	0.0669	0.467	2.93	75.7	1.06	-	-
$\bigcirc$	$\times$	11.33	0.0687	0.960	7.10	77.8	1.09	1.73	-
$\bigcirc$	$\bigcirc$	11.29	0.246	1.10	7.56	133	2.23	1.89	2.29
$(10^7 + 10^6)M_\odot$									
$\times$	$\times$	9.629	0.0493	0.253	1.49	82.3	2.15	-	-
$\bigcirc$	$\times$	4.061	0.0495	0.839	6.26	82.8	2.16	1.89	-
$\bigcirc$	$\bigcirc$	4.052	0.202	0.927	6.54	159	5.01	1.94	8.27
$(10^6 + 10^6)M_\odot$									
$\times$	$\times$	12.41	0.00869	0.122	0.787	3.01	0.316	-	-
$\bigcirc$	$\times$	3.582	0.00871	0.926	6.97	3.01	0.316	1.68	-
$\bigcirc$	$\bigcirc$	3.582	0.0288	0.933	7.00	4.75	0.589	1.69	8.00
$(10^6 + 10^5)M_\odot$									
$\times$	$\times$	6.019	0.00586	0.0551	0.337	2.45	0.521	-	-
$\bigcirc$	$\times$	1.286	0.00586	0.823	6.20	2.45	0.521	1.88	-
$\bigcirc$	$\bigcirc$	1.285	0.0200	0.826	6.21	3.96	0.989	1.88	27.0

$$v_g^2 = 1 - \frac{1}{f^2 \lambda_g^2}. \quad (68)$$

Therefore, the lower gravitational frequency makes the difference between  $v_g$  and the speed of light ( $c = 1$ ) larger. This is why the heavier binaries put more stringent constraint on  $\lambda_g$ .

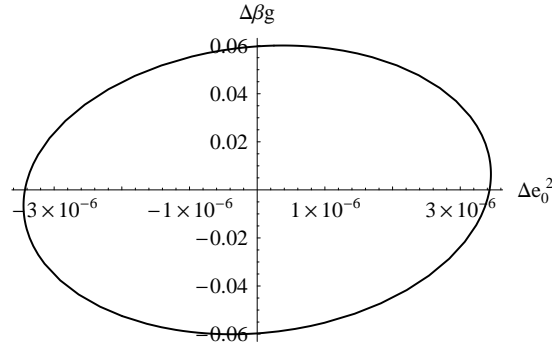


Figure 5: The curve showing constant probability on the  $\Delta e_0^2$ - $\Delta \beta_g$  plane for  $(10^7 + 10^7)M_\odot$  SMBH/BH binary at 3Gpc. The fiducial values lie at the centre of the ellipse as in Fig. 4.

### 7.1.2 Estimates without pattern-averaging

In the case of estimates without pattern-averaging, there are 13 parameters in total: the 9 parameters appeared in the last subsection and 4 angles representing the direction of the source and the inclination of the orbit. We randomly generate  $10^4$  sets of the four angles as  $\cos \theta_S$  and  $\cos \theta_L$  in the range  $[-1, 1]$



and  $\phi_S$  and  $\phi_L$  in the range  $[0, 2\pi]$ . We use the RAN1 routine [38] for generating random numbers and calculate the parameter estimation errors for each binary. We take the average at the end.

We take the parameter derivatives of the part  $e^{i\Psi(f)}$  in the waveform analytically as in the pattern-averaged case, whilst we take the derivatives of the rest numerically. The angular resolution  $\Delta\Omega_S$  is defined as

$$\Delta\Omega_S \equiv 2\pi|\sin\bar{\theta}_S|\sqrt{\Sigma_{\bar{\theta}_S\bar{\theta}_S}\Sigma_{\bar{\phi}_S\bar{\phi}_S} - \Sigma_{\bar{\theta}_S\bar{\phi}_S}^2}. \quad (69)$$

We consider the following two cases: including not  $e_0^2$  but  $\sigma$  into binary parameters, and including both  $\sigma$  and  $e_0^2$  into parameters.

Following Ref. [17], we put the results into histograms. For each binary parameter, we obtain  $10^4$  error values. We group them into  $N_{\text{bins}}$  bins as follows; if an error value  $X$  satisfies

$$\left[ \ln(X_{\min}) + \frac{(j-1)[\ln(X_{\max}) - \ln(X_{\min})]}{N_{\text{bins}}} \right] < \ln(X) < \left[ \ln(X_{\min}) + \frac{j[\ln(X_{\max}) - \ln(X_{\min})]}{N_{\text{bins}}} \right], \quad (70)$$

then we define that this belongs to the  $j$ -th bin. We divide the number of binaries of each bin by the total number of binaries 10000 to get a "probability distribution". We show this probability against the determination error of each parameter in a histogram below.

### Brans-Dicke Theory:

We fix the masses of the binary objects as  $m_{\text{NS}} = 1.4M_\odot$  and  $m_{\text{BH}} = 10^4M_\odot$ . We consider the binaries of  $\rho = \sqrt{200}$  (this corresponds to  $\rho = 10$  for each detector). We show the results in the upper half of Table 3. The first row represents the error estimation without including  $e_0^2$  as a fitting parameter and the second row shows the one including  $e_0^2$ . The corresponding histograms are shown in Fig. 6, Fig. 7 and Fig. 8. The (green) dotted-dashed line represents the results without including  $e_0^2$  as a binary parameter and the (blue) dashed line shows the one including  $e_0^2$ . The (purple) dotted and the (red) solid lines are the ones including precession, which are to be explained later. For the moment, let us focus on the (green) dotted-dashed and the (blue) dashed lines only. Figure 6 is the histogram of the lower bound of  $\omega_{\text{BD}}$ . Including  $e_0^2$  increases the error by a factor of 4, as expected from the results of pattern-averaged estimation. Figure 7 shows the histograms of  $\Delta\mathcal{M}/\mathcal{M}$ ,  $\Delta\eta/\eta$ ,  $\Delta\beta$  and  $\Delta\sigma$ . These accuracies also get worse by several factors when  $e_0^2$  are taken into account. Figure 8 shows the histograms of  $\Delta D_L/D_L$  and  $\Delta\Omega_S$ . The error estimations of  $\Delta D_L/D_L$  with and without including precession are shown separately. The (green) dotted-dashed and (blue) dashed lines in the histogram of  $\Delta D_L/D_L$  are almost the same. As  $D_L$  appears only in the amplitude of the waveform, this parameter is uncorrelated with the phase parameters such as  $e_0^2$ . The histograms of  $\Delta D_L/D_L$  have tails on the lower accuracy side. These tails are due to the binaries with  $\hat{\mathbf{L}} \cdot \hat{\mathbf{N}} = \pm 1$  because then the distance and the direction of  $\hat{\mathbf{L}}$  degenerate. Again, the accuracy of  $\Delta\Omega_S$  goes down by several factors when we include  $e_0^2$ .

In Figs. 6 and 7, there are also some tails in the histograms. The ones with worse accuracy are due to the binaries with  $\hat{\mathbf{L}} \cdot \hat{\mathbf{N}} = 0$ . Figure 9 shows  $10^4$  plots of the constraints on  $\omega_{\text{BD}}$  against  $\hat{\mathbf{L}} \cdot \hat{\mathbf{N}}$ , taking eccentricity into account (these plots correspond to the (blue) dashed histogram in Fig. 6). It can be seen that the constraints get worse when the binaries become  $\hat{\mathbf{L}} \cdot \hat{\mathbf{N}} = 0$ . The constraints on  $\omega_{\text{BD}}$  against  $\theta_S$  and  $\phi_S$  are shown in Fig. 10. It is clear that binaries with some special source directions ( $\theta_S, \phi_S$ ) enhance the parameter estimation accuracy. These tails do not depend on the directions of the orbital angular momenta  $\mathbf{L}$ . We found that they are due to the motion of the detectors (the Doppler phase  $\varphi_D(t)$ ). In Figs. 11 and 12, we show the same plots but without including the Doppler phase. It is clear that the strange peaks have disappeared in this case. The comparison of the constraint on  $\omega_{\text{BD}}$  in both cases suggest that the degeneracies among some parameters become strong when we include  $\varphi_D$ . However, these degeneracies are solved in some special cases which correspond to the peaks in Fig. 10. For example, the reason why  $\bar{\theta}_S = \frac{\pi}{2}$  is special can be understood as follows. Since  $\varphi_D(t)$  is proportional to  $\sin\bar{\theta}_S$ , the derivative of  $\varphi_D$  with respect to  $\bar{\theta}_S$  is proportional to  $\cos\bar{\theta}_S$ . Therefore when  $\bar{\theta}_S = \frac{\pi}{2}$ , this term vanishes and there would be no degeneracy between  $\omega_{\text{BD}}$  and  $\bar{\theta}_S$  that is caused by the Doppler phase.

Table 3: The results of error estimation in Brans-Dicke theory for  $(1.4 + 1000)M_\odot$  NS/BH binaries without pattern averaging. We used two detectors for the analyses and we fixed  $\rho = \sqrt{200}$  ( $\rho = 10$  for each detector). We performed the following Monte Carlo simulations. We distribute  $10^4$  binaries, calculate the error of each parameter for each binary and take the average. The first half of the table shows the results without taking precessional effect, and the second half represents the ones including precession. The first line of each part shows the ones without taking  $e_0^2$  into parameters, whilst the second line takes this into account.  $\sigma$  is included in the parameter for all the cases.

cases	$\omega_{\text{BD}}$	$\Delta \ln \mathcal{M}$ (%)	$\Delta \ln \eta$	$\Delta \beta$	$\Delta \ln D_L$	$\Delta \Omega_S$ ( $10^{-3}\text{str}$ )	$\Delta \sigma$
<b>no precession</b>							
excluding $e_0^2$	4862	0.0395	0.143	0.108	2.53	0.419	2.18
including $e_0^2$	1061	0.106	0.241	0.481	2.54	1.05	2.44
<b>including precession</b>							
excluding $e_0^2$	7040	0.0256	0.0825	0.173	0.103	0.352	1.12
including $e_0^2$	1196	0.0924	0.0196	0.175	0.104	0.925	1.52

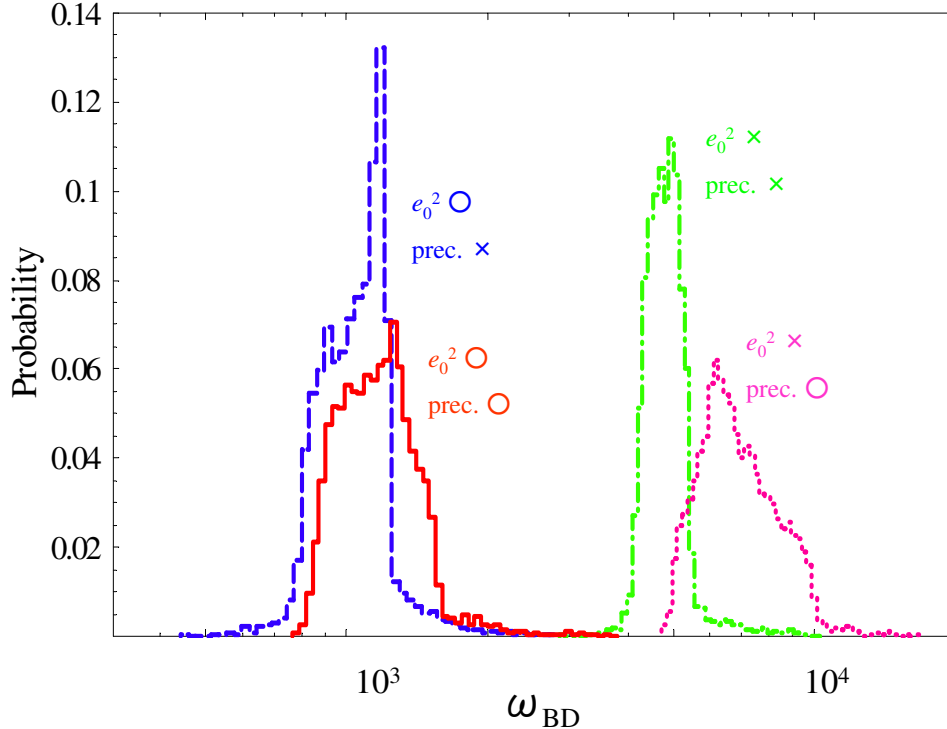


Figure 6: The histograms showing the probability distribution of the lower bound of  $\omega_{\text{BD}}$  obtained from the Monte Carlo simulations with  $(1.4 + 1000)M_\odot$  NS/BH binaries with  $\rho = \sqrt{200}$  in Brans-Dicke theory. The (green) dotted-dashed one represents the estimate without precession and  $e_0^2$  is not taken into account. The (blue) dashed one shows the one without precession but  $e_0^2$  is taken into parameters. The (purple) dotted one includes precession but does not include  $e_0^2$ . The (red) solid one shows the one including both precession and  $e_0^2$ .

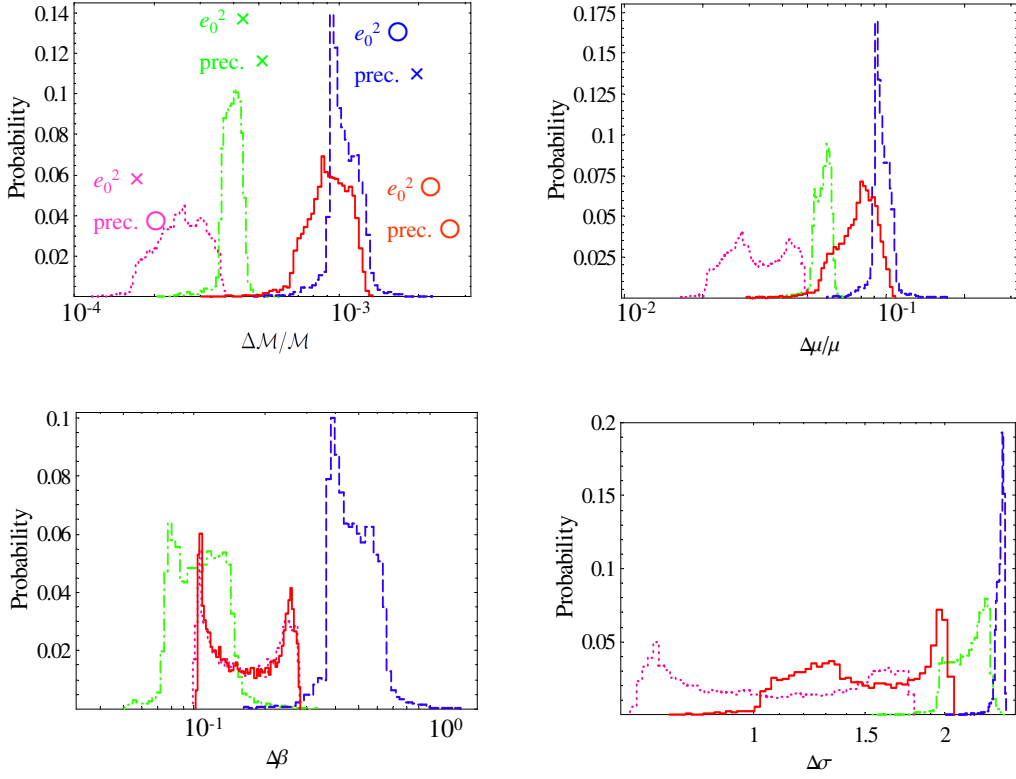


Figure 7: The histograms showing the probability distribution of the error estimates of the chirp mass  $\Delta\mathcal{M}/\mathcal{M}$ , the reduced mass  $\Delta\mu/\mu$ , the spin-orbit coupling  $\Delta\beta$  and the spin-spin coupling  $\Delta\sigma$  in Brans-Dicke theory. These are obtained from the Monte Carlo simulations with  $(1.4+1000)M_\odot$  NS/BH binaries with  $\rho = \sqrt{200}$ . The meaning of different types of curves is the same as in Fig. 6.

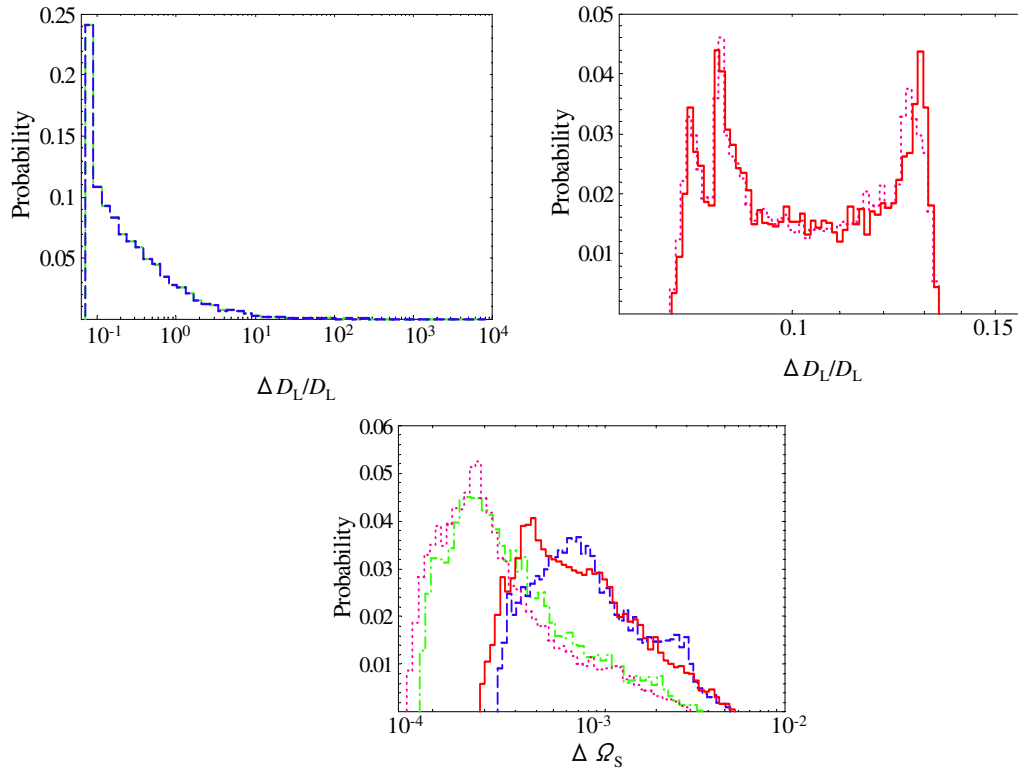


Figure 8: The histograms showing the probability distribution of the error estimates of the luminosity distance  $\Delta D_L/D_L$  and the angular resolution  $\Delta Q_s$  in Brans-Dicke theory. These are obtained from the Monte Carlo simulations with  $(1.4 + 1000)M_\odot$  NS/BH binaries with  $\rho = \sqrt{200}$ . The meaning of different types of curves is the same as in Fig. 6. The accuracy of the luminosity distance with and without precession are shown separately.

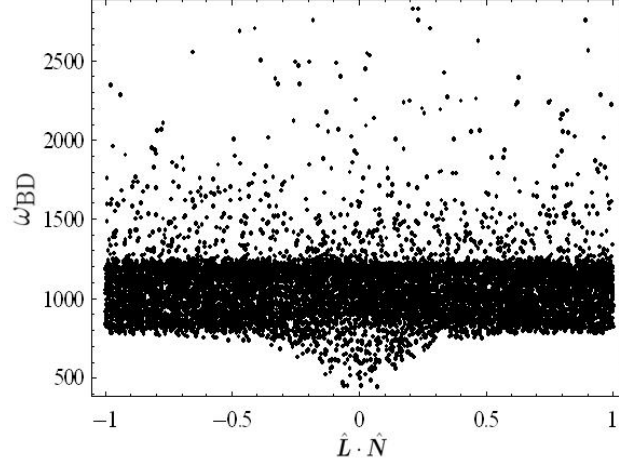


Figure 9:  $10^4$  plots of the lower bounds of  $\omega_{\text{BD}}$  against  $\hat{\mathbf{L}} \cdot \hat{\mathbf{N}}$ . This result is obtained from the Monte Carlo simulations with  $(1.4 + 1000)M_{\odot}$  NS/BH binaries with  $\rho = \sqrt{200}$  in Brans-Dicke theory.  $e_0^2$  is taken into account though the precessional effect is not included.

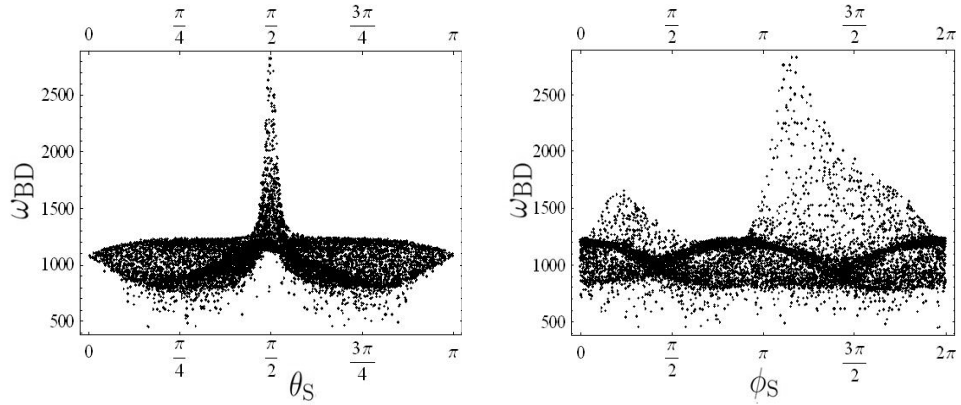


Figure 10:  $10^4$  plots of the lower bounds of  $\omega_{\text{BD}}$  against  $\bar{\theta}_S$  and  $\bar{\phi}_S$ , as in Fig. 9.

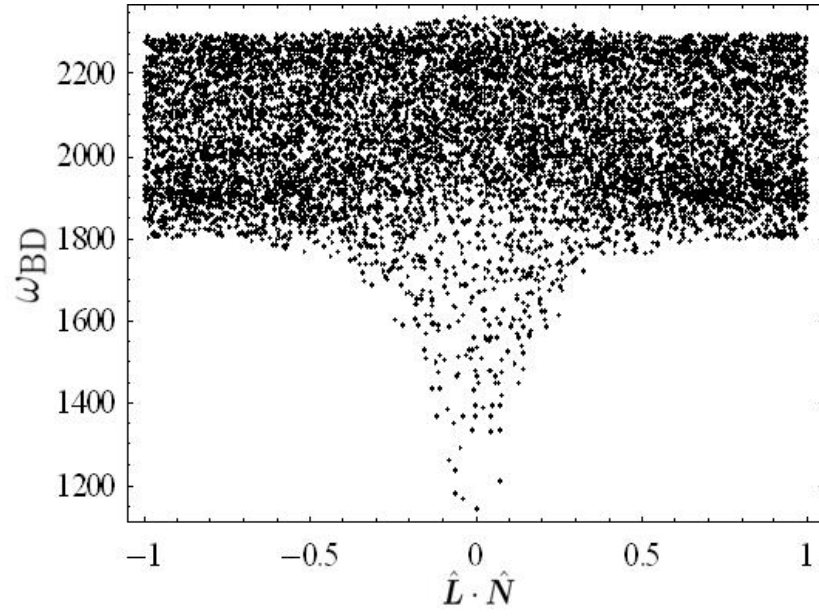


Figure 11: The same plot as Fig. 9 except we do not include the Doppler phase  $\varphi_D(t)$  in this case.

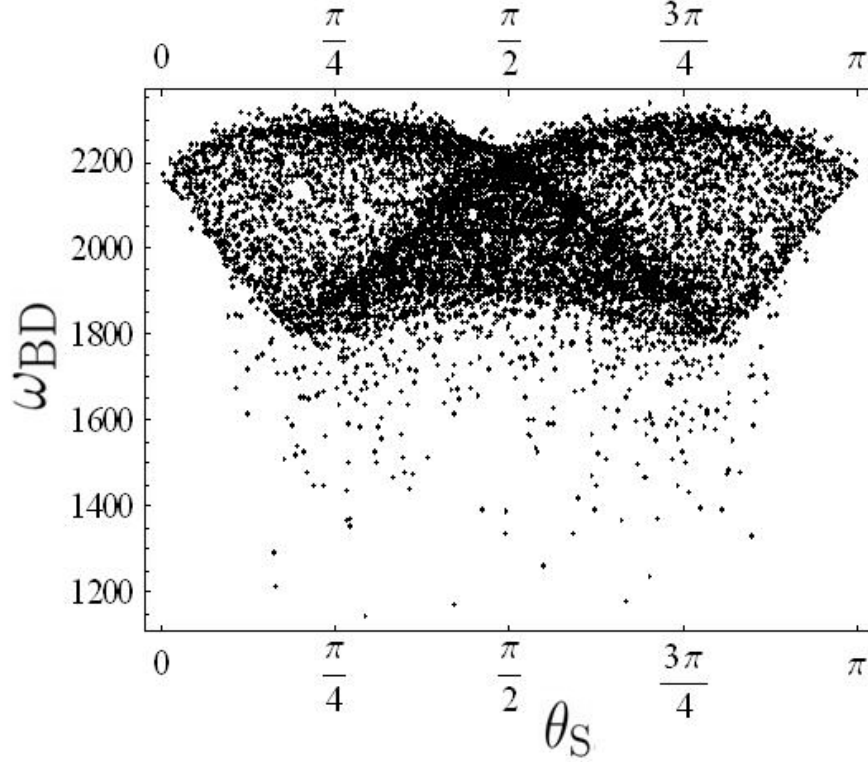


Figure 12: The same plot as Fig. 10 (only  $\bar{\theta}_S$  is shown) except we do not include the Doppler phase  $\varphi_D(t)$  in this case.

### Massive Graviton Theories:

We fix the masses of the binary objects as  $10^7 M_\odot$  and  $10^6 M_\odot$  at  $D_L = 3\text{Gpc}$ . The results are shown in the upper half of Table 4. As in the Brans-Dicke case, the first row represents the error estimation without including  $e_0^2$  into binary parameters and the second row shows the one including  $e_0^2$ . As in the Brans-Dicke case, the corresponding histograms are shown in Fig. 13 for the lower bound of  $\lambda_g$ , Fig. 14 for the error estimations of masses and spins, and Fig. 15 for the ones of the distances and the source directions. Again, the (green) dotted-dashed line represents the results without including  $e_0^2$  as a binary parameter and the (blue) dashed line shows the ones including  $e_0^2$ . In the massive graviton case, the parameter estimation is only weakly dependent on the inclusion of parameter  $e_0^2$ .

## 7.2 Including Precession

In this subsection, we show the results when we include the spin precession. There are 15 parameters in total. We perform the Monte Carlo simulations as in the previous subsection. Here, we set the dimensionless spin parameter of the lighter body of binaries to 0 and the one of the heavier body to  $\chi = 0.5$ . We also choose  $\alpha_c$  randomly in the range  $[0, 2\pi]$ . When we include the spin precession, the waveform gets some additional oscillations. This worsens the precision of the polynomial approximation to the waveform. For this reason, we decide not to use the Gauss-Legendre quadrature for the numerical integrations. Instead, we cut the integrand into  $10^4$  pieces, equally binned in terms of  $f^{-1}$ .

### Brans-Dicke theory:

We fix the masses of the binary objects as  $m_{\text{NS}} = 1.4 M_\odot$  and  $m_{\text{BH}} = 10^4 M_\odot$  of  $\rho = \sqrt{200}$ . We neglect the spins for the neutron stars, which is favoured from observations [27]. For the spins of the black holes, we adopt  $\chi = 0.5$ . The results are shown in the lower half of Table 3. The first row in this table represents

Table 4: The results of the Monte Carlo simulations in massive graviton theories for  $(10^7 + 10^6)M_\odot$  BH/BH binaries at 3Gpc without pattern averaging. We used two detectors for the analyses. As in the Brans-Dicke case, we distribute  $10^4$  binaries, calculate the error of each parameter for each binary and take the average. The meaning of each row is the same as in Table 3.

cases	$\lambda_g$ ( $10^{21}\text{cm}$ )	SNR	$\Delta \ln \mathcal{M}$ (%)	$\Delta \ln \eta$	$\Delta \beta$	$\Delta \ln D_L$	$\Delta \Omega_S$ ( $10^{-4}\text{str}$ )	$\Delta \sigma$
<b>no precession</b>								
excluding $e_0^2$	1.3051	1540	0.0340	0.151	0.882	0.0254	1.16	0.163
including $e_0^2$	1.0710	1540	0.0499	0.205	1.28	0.0269	1.30	0.283
<b>including precession</b>								
excluding $e_0^2$	4.4310	1562	0.0124	0.0244	0.0116	0.00331	0.514	0.130
including $e_0^2$	4.2445	1564	0.0138	0.0319	0.0124	0.00339	0.5444	0.184

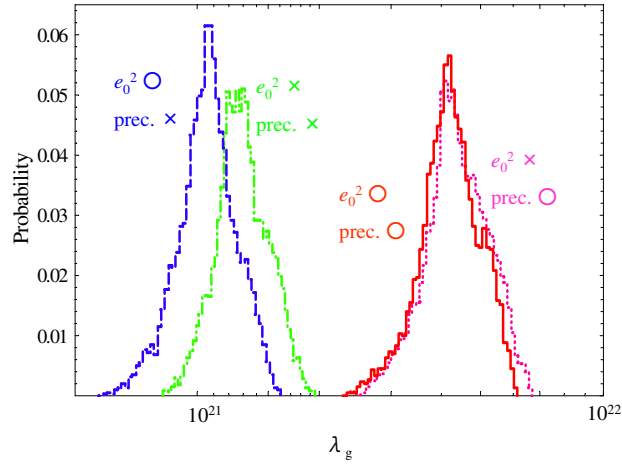


Figure 13: The histograms showing the probability distribution of the lower bound of  $\lambda_g$  obtained from the Monte Carlo simulations with  $(10^7 + 10^6)M_\odot$  BH/BH binaries at 3Gpc in massive graviton theories. The (green) dotted-dashed one represents the estimate without precession and  $e_0^2$  is not taken into account. The (purple) dotted one shows the one without precession but  $e_0^2$  is taken into parameters. The (blue) dashed one includes precession but does not take  $e_0^2$  into account. The (red) solid one shows the one including precession and  $e_0^2$  is also taken into account.



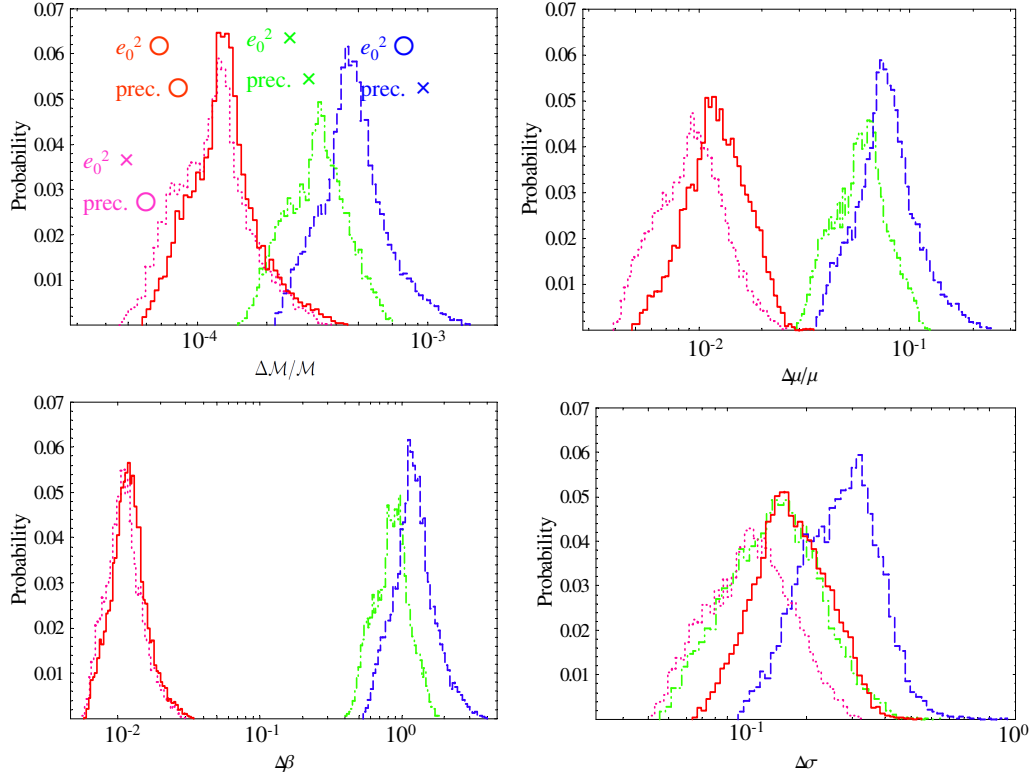


Figure 14: The histograms showing the probability distribution of the error estimates of the chirp mass  $\Delta\mathcal{M}/\mathcal{M}$ , the reduced mass  $\Delta\mu/\mu$ , the spin-orbit coupling  $\Delta\beta$  and the spin-spin coupling  $\Delta\sigma$  in massive graviton theories. These are obtained from the Monte Carlo simulations with  $(10^7 + 10^6)M_\odot$  BH/BH binaries at 3Gpc. The meaning of different types of curves is the same as in Fig. 13.

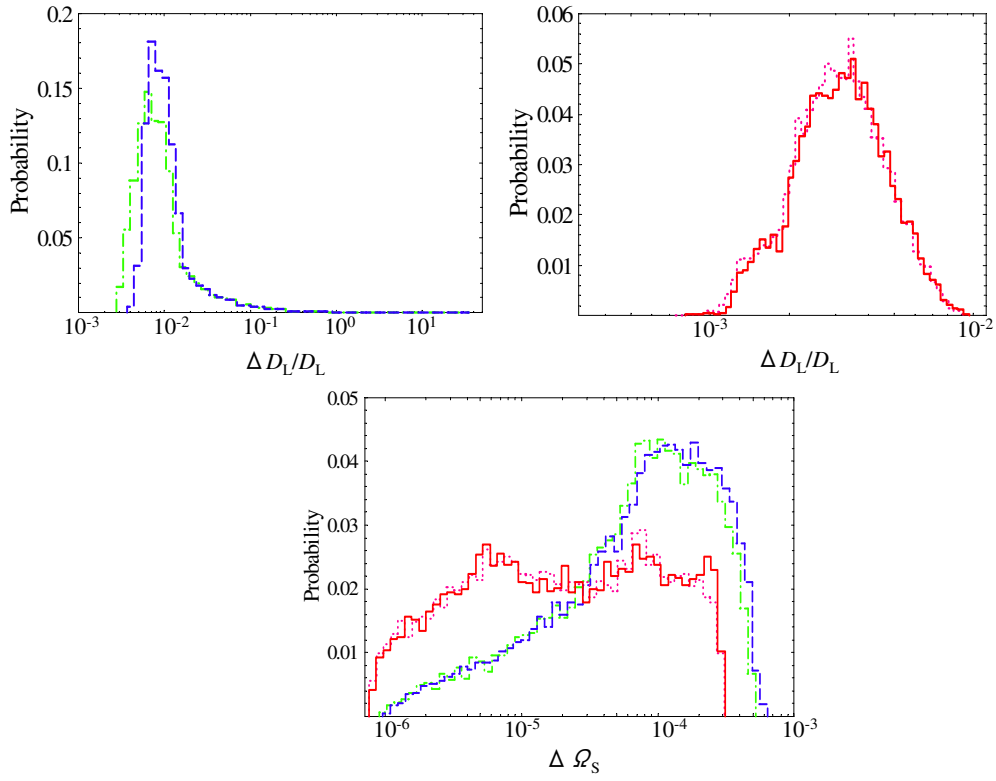


Figure 15: The histograms showing the probability distribution of the error estimates of the luminosity distance  $\Delta D_L/D_L$  and the angular resolution  $\Delta \Omega_s$  in massive graviton theories. These are obtained from the Monte Carlo simulations with  $(10^7 + 10^6)M_\odot$  BH/BH binaries at 3Gpc. The meaning of different types of curves is the same as in Fig. 13. The accuracy of the luminosity distance with and without precession are shown separately.

the results without taking eccentricity  $e_0^2$  into parameters and the second row shows the results including  $e_0^2$ . The corresponding histograms are again shown in Fig. 6, Fig. 7 and Fig. 8. The (purple) dotted line represents the estimation without taking  $e_0^2$  into parameters and the (red) solid one is the estimation with  $e_0^2$ . Figure 6 shows that the constraints on  $\omega_{\text{BD}}$  increase by 20% when the precessional effect is taken into account. In [17], Berti *et al.* found that by detecting  $(1.4 + 1000)M_\odot$  NS/BH binary gravitational waves of  $\rho = \sqrt{200}$  with LISA, one can put  $\omega_{\text{BD}} > 10799$  on average. Comparing this result with our result, it is understood that including the effects of  $\sigma$ ,  $e_0^2$  and precession, in total, leads to weaken the constraint by an order of magnitude. Therefore these effects cannot be neglected. However, as we stated before, imposing the prior  $\Delta e_0^2 > 0$  would reduce the upper limit of  $\Delta\bar{\omega}$  to the case without including  $e_0^2$  into parameters. This means that this prior strengthens the constraint on  $\omega_{\text{BD}}$  by a factor of 6. In this case, the constraint on  $\omega_{\text{BD}}$  becomes  $\omega_{\text{BD}} > 7040$  which is just 1.5 times lower than the one obtained in [17]. In Fig. 7, one can see that the lower accuracy tails disappear when we include precession, as there is no binary with  $\hat{\mathbf{L}} \cdot \hat{\mathbf{N}}$  fixed to 0 due to the precession of  $\hat{\mathbf{L}}$ . Also in Fig. 8, the tails on the histograms disappear when we include precession for the same reason.

### Massive Graviton Theories:

We fix the masses of the binary objects to  $10^7 M_\odot$  and  $10^6 M_\odot$ . We assume the spins of the  $10^6 M_\odot$  black holes to be 0 for simplicity. As in the case of Brans-Dicke theory, we take the spins of heavier black holes to be  $\chi = 0.5$ . Under this assumption, we can apply the simple precession. The results are shown in the second half of Table 4. The third row in this table represents the results without taking eccentricity  $e_0^2$  into parameters and the fourth row shows the ones including  $e_0^2$ . The corresponding histograms are shown in Fig. 13, Fig. 14 and Fig. 15. The (purple) dotted line represents the estimation without taking  $e_0^2$  into parameters and the (red) solid one is the estimation with  $e_0^2$ . In Fig. 13, it is shown that the lower bound on  $\lambda_g$  increases by a factor of 4 when we include precessional effect. Compared to the result of [17], which states that the detection of  $(10^6 + 10^6)M_\odot$  BH/BH inspiral gravitational waves with LISA leads to the constraint  $\lambda_g > 1.33 \times 10^{21} \text{cm}$  on average, our result shows that the inclusion of  $\sigma$ ,  $e_0^2$  and the precessional effect in total enhances the constraint by a factor of 3. In this case, since the parameter estimation only depends weakly on  $\sigma$  and  $e_0^2$ , the important point is to include the precession which makes the constraint stronger. Figure 14 shows that the inclusion of precession considerably enhances the accuracy of  $\Delta\mu/\mu$  and  $\Delta\beta$ , by one and two orders of magnitude respectively. In Fig. 15, one can see again that the tails on  $\Delta D_L/D_L$  disappear due to the change in  $\hat{\mathbf{L}}$ .

## 8 CONCLUSIONS

In this paper, we extended the previous analysis by Berti *et al.* [17] to see how the inclusion of the spin-spin coupling  $\sigma$ , the small eccentricity  $e_0$  and the precessional effect affects the binary parameter estimation by means of LISA in the context of alternative theories of gravity such as the Brans-Dicke and massive graviton theories. For the Brans-Dicke case, we assume that we detect NS/BH inspiral gravitational waves of  $\text{SNR}=\sqrt{200}$  because the binaries composed of different types of compact objects enhance the gravitational dipole radiation. On the other hand, we think of BH/BH inspiral gravitational waves at 3Gpc for the massive graviton case because the remarkable difference between  $v_g$  and  $c$  appears in lower frequency GWs.

First, we performed the analysis using the pattern-averaged waveform. For the error estimation in Brans-Dicke theory, the inclusion of both  $\sigma$  and  $e_0^2$  into parameters reduces the determination accuracy by an order of magnitude. Especially, including  $e_0^2$  affects the estimation more than including just  $\sigma$ . However, if we impose the prior  $\Delta e_0^2 > 0$ , the constraint becomes stronger and would be the same as the one without including  $e_0^2$  into parameters. For the analysis in the massive graviton theories, the inclusion of these parameters only changes the results by a factor of a few. In this case, the inclusion of  $\sigma$  affects more than the inclusion of  $e_0^2$ . Also in the massive gravity case, imposing the prior  $\Delta e_0^2$  would not affect the constraint on  $\lambda_g$ .

Next, we performed the Monte Carlo simulations including precession. We set the spin of the lighter body of binaries to 0 and the one of the heavier body to  $\chi = 0.5$ , which corresponds to setting the Kerr parameter to the half of mass in the black hole case. We found that in Brans-Dicke case, the results are not so much affected by taking precession into account. For NS/BH binaries of  $(1.4 + 1000)M_\odot$  with

$\text{SNR}=\sqrt{200}$ , estimation with taking  $\sigma$  and precession into account can constrain  $\omega_{\text{BD}} > 7040$  on average ( $e_0^2$  is not important for the constraint on  $\omega_{\text{BD}}$  because of the prior on  $e_0^2$ ). However, when we consider the event rate, the detectability of  $(1.4 + 1000)M_\odot$  binaries of  $\text{SNR}=\sqrt{200}$  is very low. Therefore only a lucky detection can constrain  $\omega_{\text{BD}}$ . For example, referring to Brown *et al.* [39], the event rate for EMRI is given by  $0.7 \times (300M_\odot/M) \times 10^{-10} \text{Mpc}^{-3} \text{yr}^{-1}$ . The distance of  $(1.4 + 1000)M_\odot$  binaries of  $\text{SNR}=\sqrt{200}$  corresponds to about 40Mpc for LISA. Therefore the event rate is  $7.6 \times 10^{-7} \text{yr}^{-1}$ . However for DECIGO and BBO, the event rate of NS/stellar mass BH binaries of  $\text{SNR}=\sqrt{200}$  is about  $10^4/\text{yr}$  (see [40] and references therein). Therefore, these binaries are thought to be the definite sources for them. By using these detectors, we will obtain more strong constraint [41]. This is because the number of gravitational cycles

$$N_{\text{GW}} \equiv \int_{f_{\text{in}}}^{f_{\text{fin}}} df \frac{f}{\dot{f}}, \quad (71)$$

is larger. Also the noise levels of DECIGO and BBO are lower than that of LISA. If we consider the binaries whose event rate is 1/yr for DECIGO and BBO, the sources are expected to have a large signal-to-noise ratio and we can put a few orders of magnitude stronger constraint than the solar system experiment.

In the case of massive graviton theory, inclusion of precession has more remarkable effect. The constraint on  $\lambda_g$  now becomes 4 times stronger. For BH/BH binaries of  $(10^7 + 10^6)M_\odot$  at 3Gpc, estimation with taking  $\sigma$ ,  $e_0^2$  and precession into account can constrain  $\lambda_g > 4.24 \times 10^{21} \text{cm}$  on average. This is 3 times stronger than the result obtained in Ref. [17]. In the massive graviton case, the constraint on  $\lambda_g$  obtained by DECIGO and BBO is weaker than the one obtained using LISA as larger mass binaries put stronger constraint [41].

In our calculation, we neglected the spin of one of the binaries. To make our analysis more general, we need to take the spins of both binary stars into account. In that case, because the simple precession cannot be applied anymore, we need to solve the precession equations as Stavridis and Will did [28]. We can also improve our analysis by introducing higher harmonics to the waveform. Recently, Arun and Will [42] estimated the possible constraint on  $\lambda_g$  using the higher harmonics waveform, assuming that they detect the SMBH/BH inspiral GWs with LISA, advanced LIGO and ET. Since they did not take spins into account, we should try to include both precession and higher harmonics into analysis together, and perform the Monte Carlo simulations in the alternative theories of gravity such as the Brans-Dicke and the massive graviton theories.

## ACKNOWLEDGMENTS

We thank Naoki Seto and Takashi Nakamura for useful discussions and numerical code corrections, and Bernard Schutz for valuable comments. This work is in part supported by the Grant-in-Aid for Scientific Research Nos. 19540285 and 21244033. This work is also supported in part by the Grant-in-Aid for the Global COE Program “The Next Generation of Physics, Spun from Universality and Emergence” from the Ministry of Education, Culture, Sports, Science and Technology (MEXT) of Japan.

## A CALCULATION OF THE ECCENTRICITY $e_0$

In this section, we explain the values  $e_0^2$  in our calculation. According to Peters [19], the evolution equations for the semi-major axis  $a$  and the eccentricity  $e$  of the orbit are given by

$$\frac{da}{dt} = -\frac{64}{5} \frac{m_1 m_2 M}{a^3 (1 - e^2)^{7/2}} \left( 1 + \frac{73}{24} e^2 + \frac{37}{96} e^4 \right), \quad (72)$$

$$\frac{de}{dt} = -\frac{304}{15} e \frac{m_1 m_2 M}{a^4 (1 - e^2)^{5/2}} \left( 1 + \frac{121}{304} e^2 \right). \quad (73)$$

Dividing Eq. (72) by Eq. (73), we get

$$\frac{da}{a} = \frac{19}{12} \frac{1 + \frac{73}{24} e^2 + \frac{37}{96} e^4}{e(1 - e^2)(1 + \frac{121}{304} e^2)} de. \quad (74)$$

Table 5: LISA

binary mass $e_0^2 (f_0=0.3\text{Hz})$	$(1.4 + 400)M_\odot$ $3.75 \times 10^{-10}$	$(1.4 + 400)M_\odot$ $2.31 \times 10^{-10}$	$(1.4 + 400)M_\odot$ $9.87 \times 10^{-11}$	$(1.4 + 400)M_\odot$ $6.84 \times 10^{-11}$
binary mass $e_0^2 (f_0 = 10^{-4}\text{Hz})$	$(10^7 + 10^7)M_\odot$ $1.76 \times 10^{-10}$	$(10^7 + 10^6)M_\odot$ $9.31 \times 10^{-10}$	$(10^6 + 10^6)M_\odot$ $3.68 \times 10^{-9}$	$(10^6 + 10^5)M_\odot$ $1.94 \times 10^{-8}$

Then, we integrate this equation to give

$$\frac{a}{a_i} = \frac{1 - e_i^2}{1 - e^2} \left( \frac{e}{e_i} \right)^{12/19} \left[ \frac{1 + \frac{121}{304}e^2}{1 + \frac{121}{304}e_i^2} \right], \quad (75)$$

where the subscript  $i$  denotes the value at the initial time. When  $a/a_i \ll 1$ , Eq. (75) becomes

$$e \sim \left( \frac{a}{a_i(1 - e_i^2)} \right)^{19/12} e_i. \quad (76)$$

Next, we calculate the coalescence time  $t_c(a_i, e_i)$ . This can be derived from substituting Eq. (75) into Eq. (73), taking the reciprocal and performing the integration with  $e$  from 0 to  $e_i$ ,

$$\begin{aligned} t_c(a_i, e_i) &\equiv \int_{e_i}^0 \frac{dt}{de} \\ &= \frac{15}{304} \frac{a_i^4}{m_1 m_2 M} e_i^{-48/19} \frac{(1 - e_i^2)^4}{(1 + \frac{121}{304}e_i^2)^{\frac{3480}{2299}}} \int_0^{e_i} e^{29/19} \frac{(1 + \frac{121}{304}e^2)^{\frac{1181}{2299}}}{(1 - e^2)^{3/2}} de. \end{aligned} \quad (77)$$

In the limit of  $e_i \rightarrow 0$ , the equation above reduces to

$$\begin{aligned} t_c(a_i) &= \frac{15}{304} \frac{a_i^4}{m_1 m_2 M} e_i^{-48/19} \int_0^{e_i} e^{29/19} de \\ &= \frac{5}{256} \frac{a_i^4}{m_1 m_2 M}. \end{aligned} \quad (78)$$

Then, Eq. (77) can be expressed as

$$t_c(a_i, e_i) = t_c(a_i) \frac{48}{19} e_i^{-48/19} \frac{(1 - e_i^2)^4}{(1 + \frac{121}{304}e_i^2)^{\frac{3480}{2299}}} \int_0^{e_i} e^{29/19} \frac{(1 + \frac{121}{304}e^2)^{\frac{1181}{2299}}}{(1 - e^2)^{3/2}} de. \quad (79)$$

When  $e_i \sim 1$ , this equation can be written as

$$t_c(a_i, e_i) \approx t_c(a_i)(1 - e_i^2)^{7/2}. \quad (80)$$

From these equations, we can calculate the eccentricity  $e_0$  at  $f = f_0$  for the binary whose initial eccentricity is  $e_i \sim 1$  and coalesces in the age of the universe. From Eqs. (78) and (80), we get

$$a_0 \simeq \left( \frac{256}{5} \frac{t_c \mu M^2}{(1 - e_0^2)^{7/2}} \right)^{1/4}. \quad (81)$$

When  $e_0 \ll 1$ , we can replace the semi-major axis  $a(t)$  by the orbital separation  $r(t)$ . Then, we obtain our value  $e_0$  by substituting the above equation into Eq. (76). The values  $e_0^2$  for binaries having different mass are listed in Table 5.

## B DETECTED SIGNALS

The detector having three arms corresponds to having two individual interferometers. Therefore, it is possible to measure both polarisations with one detector. We first focus on the detector I which consists of the arms 1 and 2. This detector measures

$$h_I(t) \equiv \frac{\delta L_1(t) - \delta L_2(t)}{L} = \frac{\sqrt{3}}{2} \left( \frac{1}{2} h_{xx} - \frac{1}{2} h_{yy} \right), \quad (82)$$

where  $\delta L_1(t)$  and  $\delta L_2(t)$  are the differences in length in arms 1 and 2 as caused by passing gravitational waves.  $L$  is the length of the arms where gravitational waves are not present. The factor  $\sqrt{3}/2$  comes from the  $60^\circ$  opening angle of adjacent arms. Here, we introduce two principal axes for the wave;  $\hat{\mathbf{p}} = \hat{\mathbf{N}} \times \hat{\mathbf{L}} / |\hat{\mathbf{N}} \times \hat{\mathbf{L}}|$  and  $\hat{\mathbf{q}} = \hat{\mathbf{p}} \times \hat{\mathbf{N}}$ , where  $\hat{\mathbf{L}}$  is the unit vector parallel to the orbital angular momentum and  $\hat{\mathbf{N}}$  is the unit vector pointing toward the centre of mass of the binary. Then, the two polarisations become exactly  $\pi/2$  out of phase and the waveform becomes

$$h_{ab}(t) = A_+ H_{ab}^+ \cos \phi(t) + A_\times H_{ab}^\times \sin \phi(t), \quad (83)$$

where  $H_{ab}^+$  and  $H_{ab}^\times$  are the polarisation basis tensors, defined as

$$H_{ab}^+ = p_a p_b - q_a q_b, \quad H_{ab}^\times = p_a q_b + q_a p_b. \quad (84)$$

From Eq. (82)-Eq. (84), the detector output  $h_I(t)$  becomes

$$h_I(t) = \frac{\sqrt{3}}{2} A_+ F_I^+(\theta_S, \phi_S, \psi_S) \cos \phi(t) + \frac{\sqrt{3}}{2} A_\times F_I^\times(\theta_S, \phi_S, \psi_S) \sin \phi(t). \quad (85)$$

$F_I^+(\theta_S, \phi_S, \psi_S)$  and  $F_I^\times(\theta_S, \phi_S, \psi_S)$  are the detector beam pattern coefficients and when the detector is an interferometer, they are given by

$$F_I^+(\theta_S, \phi_S, \psi_S) = \frac{1}{2} (1 + \cos^2 \theta_S) \cos(2\phi_S) \cos(2\psi_S) - \cos(\theta_S) \sin(2\phi_S) \sin(2\psi_S), \quad (86)$$

$$F_I^\times(\theta_S, \phi_S, \psi_S) = \frac{1}{2} (1 + \cos^2 \theta_S) \cos(2\phi_S) \sin(2\psi_S) + \cos(\theta_S) \sin(2\phi_S) \cos(2\psi_S). \quad (87)$$

$(\theta_S, \phi_S)$  represents the direction of the source in the detector frame and  $\psi_S$  is the polarisation angle defined as

$$\tan \psi_S = \frac{\hat{\mathbf{q}} \cdot \hat{\mathbf{z}}}{\hat{\mathbf{p}} \cdot \hat{\mathbf{z}}} = \frac{\hat{\mathbf{L}} \cdot \hat{\mathbf{z}} - (\hat{\mathbf{L}} \cdot \hat{\mathbf{N}})(\hat{\mathbf{z}} \cdot \hat{\mathbf{N}})}{\hat{\mathbf{N}} \cdot (\hat{\mathbf{L}} \times \hat{\mathbf{z}})}. \quad (88)$$

Also, we can think of another detector consisting of arms 2 and 3. We call this detector II' and the signal of this detector can be written as  $h_{II'} = (\delta L_2(t) - \delta L_3(t))/L$ . However, since  $h_I$  and  $h_{II'}$  have some correlations, they are not independent detectors. We combine detectors I and II' to construct detector II which is uncorrelated with detector I. The signal of detector II is

$$h_{II}(t) \equiv \frac{1}{\sqrt{3}} [h_I(t) + 2h_{II'}(t)] = \frac{\sqrt{3}}{2} \left[ \frac{1}{2} (h_{xy} + h_{yx}) \right]. \quad (89)$$

This detector II corresponds to an interferometer that is rotated by  $45^\circ$  with respect to detector I. Thus the beam pattern coefficients for the detector II are

$$F_{II}^+(\theta_S, \phi_S, \psi_S) = F_I^+(\theta_S, \phi_S - \pi/4, \psi_S), \quad (90)$$

$$F_{II}^\times(\theta_S, \phi_S, \psi_S) = F_I^\times(\theta_S, \phi_S - \pi/4, \psi_S). \quad (91)$$

Reexpressing the waveforms measured by each detector in terms of an amplitude and phase, they become Eq. (19).

When we perform parameter estimation, we take the direction of the source  $(\bar{\theta}_S, \bar{\phi}_S)$  and the direction of the orbital angular momentum  $(\bar{\theta}_L, \bar{\phi}_L)$ , both measured in the solar barycentric frame, as binary parameters. Therefore we need to express the waveforms (especially  $\hat{\mathbf{L}} \cdot \hat{\mathbf{N}}$  and the beam-pattern functions  $F_\alpha^+$  and  $F_\alpha^\times$  which appear in Eqs. (20)-(22)) in terms of  $\bar{\theta}_S, \bar{\phi}_S, \bar{\theta}_L$  and  $\bar{\phi}_L$ .  $\theta_S(t)$  and  $\phi_S(t)$  are expressed as

$$\cos \theta_S(t) = \frac{1}{2} \cos \bar{\theta}_S - \frac{\sqrt{3}}{2} \sin \bar{\theta}_S \cos[\bar{\phi}(t) - \bar{\phi}_S], \quad (92)$$

$$\phi_S(t) = \alpha_1 + \frac{\pi}{12} + \tan^{-1} \left( \frac{\sqrt{3} \cos \bar{\theta}_S + \sin \bar{\theta}_S \cos[\bar{\phi}(t) - \bar{\phi}_S]}{2 \sin \bar{\theta}_S \sin[\bar{\phi}(t) - \bar{\phi}_S]} \right). \quad (93)$$

For the polarisation angle  $\psi_S$  (see Eq. (88)), first  $\hat{\mathbf{z}} \cdot \hat{\mathbf{N}} = \cos \theta_S$ . Next when we neglect the spin precessional effects,  $\hat{\mathbf{L}}$  is constant and  $\hat{\mathbf{L}} \cdot \hat{\mathbf{z}}$ ,  $\hat{\mathbf{L}} \cdot \hat{\mathbf{N}}$  and  $\hat{\mathbf{N}} \cdot (\hat{\mathbf{L}} \times \hat{\mathbf{z}})$  are given as

$$\hat{\mathbf{L}} \cdot \hat{\mathbf{z}} = \frac{1}{2} \cos \bar{\theta}_L - \frac{\sqrt{3}}{2} \sin \bar{\theta}_L \cos[\bar{\phi}(t) - \bar{\phi}_L], \quad (94)$$

$$\hat{\mathbf{L}} \cdot \hat{\mathbf{N}} = \cos \bar{\theta}_L \cos \bar{\theta}_S + \sin \bar{\theta}_L \sin \bar{\theta}_S \cos(\bar{\phi}_L - \bar{\phi}_S), \quad (95)$$

$$\begin{aligned} \hat{\mathbf{N}} \cdot (\hat{\mathbf{L}} \times \hat{\mathbf{z}}) &= \frac{1}{2} \sin \bar{\theta}_L \sin \bar{\theta}_S \sin(\bar{\phi}_L - \bar{\phi}_S) \\ &\quad - \frac{\sqrt{3}}{2} \cos \bar{\phi}(t) (\cos \bar{\theta}_L \sin \bar{\theta}_S \sin \bar{\phi}_S - \cos \bar{\theta}_S \sin \bar{\theta}_L \sin \bar{\phi}_L) \\ &\quad - \frac{\sqrt{3}}{2} \sin \bar{\phi}(t) (\cos \bar{\theta}_S \sin \bar{\theta}_L \cos \bar{\phi}_L - \cos \bar{\theta}_L \sin \bar{\theta}_S \cos \bar{\phi}_S). \end{aligned} \quad (96)$$

## C THE ANALYTIC FORMULA FOR THE ORBITAL ANGULAR MOMENTUM $\mathbf{L}$ UNDER SIMPLE PRECESSION

The precession equations for circular orbit binaries are [26]

$$\begin{aligned} \dot{\mathbf{L}} &= \frac{1}{r^3} \left[ \frac{4m_1 + 3m_2}{2m_1} \mathbf{S}_1 + \frac{4m_2 + 3m_1}{2m_2} \mathbf{S}_2 \right] \times \mathbf{L} \\ &\quad - \frac{3}{2} \frac{1}{r^3} [(\mathbf{S}_2 \cdot \hat{\mathbf{L}}) \mathbf{S}_1 + (\mathbf{S}_1 \cdot \hat{\mathbf{L}}) \mathbf{S}_2] \times \hat{\mathbf{L}} - \frac{32}{5} \frac{\mu^2}{r} \left( \frac{M^{5/2}}{r} \right) \hat{\mathbf{L}}, \end{aligned} \quad (97)$$

$$\dot{\mathbf{S}}_1 = \frac{1}{r^3} \left[ \frac{4m_1 + 3m_2}{2m_1} (\mu \sqrt{Mr} \hat{\mathbf{L}}) \right] \times \mathbf{S}_1 + \frac{1}{r^3} \left[ \frac{1}{2} \mathbf{S}_2 - \frac{3}{2} (\mathbf{S}_2 \cdot \hat{\mathbf{L}}) \hat{\mathbf{L}} \right] \times \mathbf{S}_1, \quad (98)$$

$$\dot{\mathbf{S}}_2 = \frac{1}{r^3} \left[ \frac{4m_2 + 3m_1}{2m_2} (\mu \sqrt{Mr} \hat{\mathbf{L}}) \right] \times \mathbf{S}_2 + \frac{1}{r^3} \left[ \frac{1}{2} \mathbf{S}_1 - \frac{3}{2} (\mathbf{S}_1 \cdot \hat{\mathbf{L}}) \hat{\mathbf{L}} \right] \times \mathbf{S}_2. \quad (99)$$

The first term of each equation represents the spin-orbit interactions (1.5PN) and the second term represents the spin-spin interactions (2PN). The last term of Eq. (97) is the angular momentum loss due to the radiation reaction. This changes the total angular momentum  $\mathbf{J} \equiv \mathbf{L} + \mathbf{S}_1 + \mathbf{S}_2$  as

$$\dot{\mathbf{J}} = -\frac{32}{5} \frac{\mu^2}{r} \left( \frac{M^{5/2}}{r} \right) \hat{\mathbf{L}}. \quad (100)$$

In this paper, we assume that one of the spins of the binary objects is negligible (i.e.  $\mathbf{S}_1 \sim 0$ ). Then, there do not exist spin-spin interactions. We also assume that the orbital angular momentum  $\mathbf{L}$  is neither parallel nor antiparallel to the total spin angular momentum  $\mathbf{S} (= \mathbf{S}_1 + \mathbf{S}_2)$ . Then, the precession equations are simplified and  $\hat{\mathbf{L}}$  is obtained analytically up to some approximate orders. This is the so-called *simple precession* [26]. This also holds when the masses of the binary objects are equal

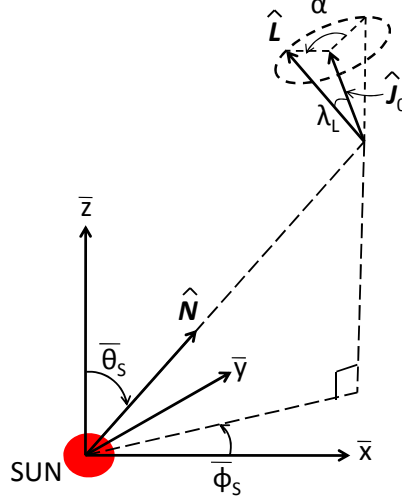


Figure 16: The unit orbital angular momentum vector  $\hat{\mathbf{L}}$  precesses around a fixed vector  $\hat{\mathbf{J}}_0$ . The opening angle of the precession cone is given by  $\lambda_L$  and the precession angle is denoted as  $\alpha$ .

( $m_1 \sim m_2$ ) and spin-spin interactions are negligible, instead of  $\mathbf{S}_1 \sim 0$ . Under this simple precession, the precession equations become Eq. (30)-(33).

Next, we define a quantity  $\gamma(t)$  as

$$\gamma(t) \equiv \frac{S}{L(t)}. \quad (101)$$

Then, the magnitude and the direction of the total angular momentum  $\mathbf{J}$  can be expressed in terms of  $\kappa$ ,  $\gamma(t)$ ,  $L(t)$ ,  $\hat{\mathbf{L}}$  and  $\hat{\mathbf{S}}$ ,

$$J = L\sqrt{1 + 2\kappa\gamma + \gamma^2}, \quad (102)$$

$$\hat{\mathbf{J}} = \frac{\hat{\mathbf{L}} + \gamma\hat{\mathbf{S}}}{\sqrt{1 + 2\kappa\gamma + \gamma^2}}. \quad (103)$$

From Eqs. (32), (33) and (103), the precession equation of  $\hat{\mathbf{J}}$  can be derived as

$$\dot{\hat{\mathbf{J}}} = \frac{\dot{\gamma}[\hat{\mathbf{S}}(1 + \kappa\gamma) - \hat{\mathbf{L}}(\kappa + \gamma)]}{(1 + 2\kappa\gamma + \gamma^2)^{3/2}}. \quad (104)$$

From Eqs. (32) and (33), it can be seen that the vectors  $\hat{\mathbf{L}}$  and  $\hat{\mathbf{S}}$  precess around  $\hat{\mathbf{J}}$  with the angular velocity  $\Omega_p$  given as Eq. (34). In general, the precessing timescale  $\Omega_p^{-1}$  is shorter than the inspiral timescale  $L/|\dot{L}|$ . Therefore from  $\dot{\mathbf{J}} = \dot{L}\hat{\mathbf{L}}$ ,  $\mathbf{J}$  changes in magnitude but the direction is almost constant. Actually, if  $J$  is much smaller than  $L$  (as this can happen when  $\mathbf{L}$  and  $\mathbf{S}$  are antialigned with almost the same magnitudes),  $\hat{\mathbf{J}}$  can change significantly in one precessional period. Therefore, we introduce the following small parameter,

$$\varepsilon \equiv \frac{L}{J} \frac{|\dot{L}|/L}{\Omega_p} = \frac{|\dot{\mathbf{J}}|/J}{\Omega_p}. \quad (105)$$

Then,  $\mathbf{J}$  precesses around the fixed direction  $\hat{\mathbf{J}}_0$  with

$$\hat{\mathbf{J}}_0 = \hat{\mathbf{J}} - \varepsilon \hat{\mathbf{J}} \times \hat{\mathbf{L}} \quad (106)$$



up to  $O(\varepsilon^2)$ . To the same order, the precession equation for  $\hat{\mathbf{L}}$  becomes

$$\dot{\hat{\mathbf{L}}} = \Omega_p \hat{\mathbf{J}}_0 \times \hat{\mathbf{L}} + \varepsilon \Omega_p (\hat{\mathbf{J}}_0 \times \hat{\mathbf{L}}) \times \hat{\mathbf{L}}. \quad (107)$$

The solution of this equation can be obtained geometrically [26]. We take the barycentric Cartesian frame  $(\bar{x}, \bar{y}, \bar{z})$  which is tied to the ecliptic and centred in the solar system barycentre. Let the barycentre of the binary point in the  $((\bar{\theta}_S, \bar{\phi}_S))$  direction and let  $\hat{\mathbf{J}}_0$  point in the  $(\bar{\theta}_J, \bar{\phi}_J)$  direction. We denote  $\lambda_L$  as the opening angle of the cone on which  $\hat{\mathbf{L}}$  precesses (i.e. the angle between  $\hat{\mathbf{L}}$  and  $\hat{\mathbf{J}}_0$ , see Fig. 16). This can be regarded as the angle between  $\hat{\mathbf{L}}$  and  $\hat{\mathbf{J}}$  apart from the errors of order  $\varepsilon^2$  and is given by

$$\cos \lambda_L = \hat{\mathbf{L}} \cdot \hat{\mathbf{J}} = \frac{1 + \kappa\gamma}{\sqrt{1 + 2\kappa\gamma + \gamma^2}}, \quad (108)$$

$$\sin \lambda_L = \frac{|\dot{\hat{\mathbf{L}}}|}{\Omega_p} = \frac{\gamma\sqrt{1 - \kappa^2}}{\sqrt{1 + 2\kappa\gamma + \gamma^2}}. \quad (109)$$

Then,  $\hat{\mathbf{L}}$  can be expressed as

$$\hat{\mathbf{L}} = \hat{\mathbf{J}}_0 \cos \lambda_L + \frac{\hat{\mathbf{z}} - \hat{\mathbf{J}}_0 \cos \bar{\theta}_J}{\sin \bar{\theta}_J} \sin \lambda_L \cos \alpha + (\hat{\mathbf{J}}_0 \times \hat{\mathbf{z}}) \frac{\sin \lambda_L \sin \alpha}{\sin \bar{\theta}_J}, \quad (110)$$

where  $\alpha$  is the *precession angle* defined as the solution of

$$\frac{d\alpha}{dt} \equiv \Omega_p. \quad (111)$$

We assume that  $\alpha = 0$  is when  $\hat{\mathbf{L}} \cdot \hat{\mathbf{z}}$  is maximum (see Fig. 16). By solving the above equation, we get

$$\begin{aligned} \alpha = \alpha_c - \frac{5}{96} \frac{1}{\mu^3 M^3} \left( 1 + \frac{3}{4} \frac{m_1}{m_2} \right) \\ \times \left[ 2(\mathcal{G}L)^3 - 3\kappa S(L + \kappa S)\mathcal{G}L - 3\kappa S^3(1 - \kappa^2) \operatorname{arcsinh} \left( \frac{L + \kappa S}{S\sqrt{1 - \kappa^2}} \right) \right], \end{aligned} \quad (112)$$

where  $\alpha_c$  is a quantity which characterises  $\alpha$  at  $t = t_c$  and  $\mathcal{G}$  is defined as

$$\mathcal{G} \equiv \sqrt{1 + 2\kappa\gamma + \gamma^2}. \quad (113)$$

From Eq. (110), the quantities  $(\hat{\mathbf{L}} \cdot \hat{\mathbf{N}})$ ,  $(\hat{\mathbf{L}} \cdot \hat{\mathbf{z}})$  and  $[\hat{\mathbf{N}} \cdot (\hat{\mathbf{L}} \times \hat{\mathbf{z}})]$ , which are needed to compute the polarisation angle  $\psi_S(t)$  in the beam pattern coefficients  $F_\alpha^+$  and  $F_\alpha^\times$ , are expressed as [20]

$$\begin{aligned} \hat{\mathbf{L}} \cdot \hat{\mathbf{z}} &= (\hat{\mathbf{J}}_0 \cdot \hat{\mathbf{z}}) \cos \lambda_L + \frac{1 - 2(\hat{\mathbf{J}}_0 \cdot \hat{\mathbf{z}}) \cos \bar{\theta}_J}{2 \sin \bar{\theta}_J} \sin \lambda_L \cos \alpha \\ &\quad + \frac{(\hat{\mathbf{J}}_0 \times \hat{\mathbf{z}}) \cdot \hat{\mathbf{z}}}{\sin \bar{\theta}_J} \sin \lambda_L \sin \alpha, \end{aligned} \quad (114)$$

$$\begin{aligned} \hat{\mathbf{L}} \cdot \hat{\mathbf{N}} &= (\hat{\mathbf{J}}_0 \cdot \hat{\mathbf{N}}) \cos \lambda_L + \frac{\cos \bar{\theta}_S - (\hat{\mathbf{J}}_0 \cdot \hat{\mathbf{N}}) \cos \bar{\theta}_J}{\sin \bar{\theta}_J} \sin \lambda_L \cos \alpha \\ &\quad + \frac{(\hat{\mathbf{J}}_0 \times \hat{\mathbf{z}}) \cdot \hat{\mathbf{N}}}{\sin \bar{\theta}_J} \sin \lambda_L \sin \alpha, \end{aligned} \quad (115)$$

$$\begin{aligned} \hat{\mathbf{N}} \cdot (\hat{\mathbf{L}} \times \hat{\mathbf{z}}) &= \hat{\mathbf{N}} \cdot (\hat{\mathbf{J}}_0 \times \hat{\mathbf{z}}) \cos \lambda_L + \frac{\hat{\mathbf{N}} \cdot (\hat{\mathbf{z}} \times \hat{\mathbf{z}}) - \hat{\mathbf{N}} \cdot (\hat{\mathbf{J}}_0 \times \hat{\mathbf{z}}) \cos \bar{\theta}_J}{\sin \bar{\theta}_J} \sin \lambda_L \cos \alpha \\ &\quad + \frac{\hat{\mathbf{N}} \cdot (\hat{\mathbf{J}}_0 \times \hat{\mathbf{z}}) \times \hat{\mathbf{z}}}{\sin \bar{\theta}_J} \sin \lambda_L \sin \alpha, \end{aligned} \quad (116)$$

where

$$\hat{\mathbf{J}}_0 \cdot \hat{\mathbf{z}} = \frac{1}{2} \cos \bar{\theta}_J - \frac{\sqrt{3}}{2} \sin \bar{\theta}_J \cos[\bar{\phi}(t) - \bar{\phi}_J], \quad (117)$$

$$\hat{\mathbf{J}}_0 \cdot \hat{\mathbf{N}} = \cos \bar{\theta}_J \cos \bar{\theta}_S + \sin \bar{\theta}_J \sin \bar{\theta}_S \cos(\bar{\phi}_J - \bar{\phi}_S), \quad (118)$$

$$\begin{aligned} \hat{\mathbf{N}} \cdot (\hat{\mathbf{J}}_0 \times \hat{\mathbf{z}}) &= \frac{1}{2} \sin \bar{\theta}_J \sin \bar{\theta}_S \sin(\bar{\phi}_J - \bar{\phi}_S) \\ &\quad - \frac{\sqrt{3}}{2} \cos \bar{\phi}(t) (\cos \bar{\theta}_J \sin \bar{\theta}_S \sin \bar{\phi}_S - \cos \bar{\theta}_S \sin \bar{\theta}_J \sin \bar{\phi}_J) \\ &\quad - \frac{\sqrt{3}}{2} \sin \bar{\phi}(t) (\cos \bar{\theta}_S \sin \bar{\theta}_J \cos \bar{\phi}_J - \cos \bar{\theta}_J \sin \bar{\theta}_S \cos \bar{\phi}_S), \end{aligned} \quad (119)$$

$$(\hat{\mathbf{J}}_0 \times \hat{\mathbf{z}}) \cdot \hat{\mathbf{N}} = \sin \bar{\theta}_S \sin \bar{\theta}_J \sin(\bar{\phi}_J - \bar{\phi}_S), \quad (120)$$

$$\hat{\mathbf{N}} \cdot (\hat{\mathbf{z}} \times \hat{\mathbf{z}}) = \frac{\sqrt{3}}{2} \sin \bar{\theta}_S \sin(\bar{\phi}(t) - \bar{\phi}_S), \quad (121)$$

$$(\hat{\mathbf{J}}_0 \times \hat{\mathbf{z}}) \cdot \hat{\mathbf{z}} = \frac{\sqrt{3}}{2} \sin \bar{\theta}_J \sin(\bar{\phi}(t) - \bar{\phi}_J), \quad (122)$$

$$\hat{\mathbf{N}} \cdot (\hat{\mathbf{J}}_0 \times \hat{\mathbf{z}}) \times \hat{\mathbf{z}} = -\frac{1}{2} \sin \bar{\theta}_J [\sqrt{3} \cos \bar{\theta}_S \cos\{\bar{\phi}(t) - \bar{\phi}_J\} + \sin \bar{\theta}_S \cos(\bar{\phi}_J - \bar{\phi}_S)]. \quad (123)$$

When spins are zero,  $\sin \lambda_L = 0$ ,  $\bar{\theta}_J = \bar{\theta}_L$ ,  $\bar{\phi}_J = \bar{\phi}_L$ . Then, Eqs. (114), (115) and (116) each reduces to Eqs. (94), (95) and (96) respectively.

$\hat{\mathbf{L}} \cdot \hat{\mathbf{u}}$  and  $\hat{\mathbf{N}} \cdot (\hat{\mathbf{L}} \times \hat{\mathbf{u}})$  in Eq. (46) are given as follows;

$$\begin{aligned} \hat{\mathbf{L}} \cdot \hat{\mathbf{u}} &= -\hat{\mathbf{N}} \cdot (\hat{\mathbf{L}} \times \hat{\mathbf{J}}_0) \\ &= \hat{\mathbf{N}} \cdot (\hat{\mathbf{J}}_0 \times \hat{\mathbf{z}}) \frac{\sin \lambda_L}{\sin \theta_J} \cos \alpha - (\cos \theta_S - \cos \theta_J (\hat{\mathbf{J}}_0 \cdot \hat{\mathbf{N}})) \frac{\sin \lambda_L}{\sin \theta_J} \sin \alpha, \end{aligned} \quad (124)$$

$$\hat{\mathbf{N}} \cdot (\hat{\mathbf{L}} \times \hat{\mathbf{u}}) = \cos \lambda_L - (\hat{\mathbf{L}} \cdot \hat{\mathbf{N}}) \cdot (\hat{\mathbf{J}}_0 \cdot \hat{\mathbf{N}}), \quad (125)$$

where  $\hat{\mathbf{N}} \cdot (\hat{\mathbf{J}}_0 \times \hat{\mathbf{z}})$  and  $\hat{\mathbf{J}}_0 \cdot \hat{\mathbf{N}}$  are given as Eqs. (119) and (118), respectively.

## D THE INVERSION OF THE FISHER MATRIX

If the ratio (we denote this by  $R$ ) of the smallest eigenvalue to the largest one in the Fisher matrix  $\mathbf{\Gamma}$  approaches the machine's floating-point precision, the inverse of  $\mathbf{\Gamma}$  will not be performed correctly. This problem can be avoided by the following technique.

First, we define

$$\mathbf{T} \equiv \text{diag} \left( \frac{1}{\sqrt{\Gamma_{ii}}} \right). \quad (126)$$

Next, we obtain the normalised Fisher matrix  $\mathbf{\Gamma}'$  as follows;

$$\mathbf{\Gamma}' \equiv \mathbf{T} \mathbf{\Gamma} \mathbf{T}^T = \mathbf{T} \mathbf{\Gamma} \mathbf{T}. \quad (127)$$

Then, all the diagonal components of  $\mathbf{\Gamma}'$  equal to 1. After that, we take the inverse of  $\mathbf{\Gamma}'$ . From  $\mathbf{\Gamma}'^{-1} = \mathbf{T}^{-1} \mathbf{\Gamma}^{-1} \mathbf{T}^{-1}$ , we obtain the inverse of our original Fisher matrix  $\mathbf{\Gamma}$  by multiplying  $\mathbf{T}$  from both sides of  $\mathbf{\Gamma}'^{-1}$ ,

$$\mathbf{\Gamma}^{-1} = \mathbf{T} \mathbf{\Gamma}'^{-1} \mathbf{T}. \quad (128)$$

Even if the ratio  $R$  is smaller than the machine's floating point precision, the ratio for the normalised Fisher matrix  $\mathbf{\Gamma}'$  can be larger than the floating point precision so that the inversion can be performed correctly even in the double precision computation.

## E THE ANALYTIC FORMS OF $\frac{\partial \tilde{h}}{\partial \theta^a}$ USED IN THE PATTERN-AVERAGED ESTIMATES

In Sec. 7.1.1, we calculate the parameter determination errors with pattern-averaged estimates. There are 9 parameters in total:  $\ln \mathcal{M}, \ln \eta, t_c, \phi_c, D_L, \beta, \sigma, e_0$  and  $\bar{\omega}$  or  $\beta_g$ . The waveform is given by Eq. (29), where the amplitude  $\mathcal{A}$  and the phase  $\Psi(f)$  are given by Eqs. (27) and (28), respectively. The derivative of this waveform with respect to each parameter is taken analytically as [17];

$$\frac{\partial \tilde{h}}{\partial \ln \mathcal{M}} = -\frac{5i}{128}(\pi \mathcal{M} f)^{-5/3}(k_4 x^{-1} + 1 + d_4 + a_4 x + b_4 x^{3/2} + c_4 x^2) \tilde{h}, \quad (129)$$

$$\frac{\partial \tilde{h}}{\partial \ln \eta} = -\frac{i}{96}(\pi \mathcal{M} f)^{-5/3}(k_5 x^{-1} + 1 + a_5 x + b_5 x^{3/2} + c_5 x^2) \tilde{h}, \quad (130)$$

$$\frac{\partial \tilde{h}}{\partial \ln D_L} = -\tilde{h}, \quad (131)$$

$$\frac{\partial \tilde{h}}{\partial t_c} = i2\pi f \tilde{h}, \quad (132)$$

$$\frac{\partial \tilde{h}}{\partial \phi_c} = -i\tilde{h}, \quad (133)$$

$$\frac{\partial \tilde{h}}{\partial \beta} = \frac{3i}{32}(\pi \mathcal{M} f)^{-5/3} x^{3/2} \tilde{h}, \quad (134)$$

$$\frac{\partial \tilde{h}}{\partial \sigma} = -\frac{15i}{64}(\pi \mathcal{M} f)^{-5/3} x^2 \tilde{h}, \quad (135)$$

$$\frac{\partial \tilde{h}}{\partial e_0^2} = -\frac{7065i}{187136}(\pi \mathcal{M} f)^{-5/3} f_0^{19/9} f^{-19/9} \tilde{h}, \quad (136)$$

$$\frac{\partial \tilde{h}}{\partial \bar{\omega}} = -\frac{5i}{3584} \mathcal{S}^2 (\pi \mathcal{M} f)^{-5/3} x^{-1} \tilde{h}, \quad (137)$$

$$\frac{\partial \tilde{h}}{\partial \beta_g} = -i(\pi \mathcal{M} f)^{-1} \tilde{h}, \quad (138)$$

where

$$a_4 = \frac{4}{3} \left( \frac{743}{336} + \frac{11}{4} \eta \right) - \frac{128}{5} \beta_g \eta^{2/5}, \quad (139)$$

$$b_4 = \frac{8}{5}(\beta - 4\pi), \quad (140)$$

$$c_4 = 2 \left( \frac{3058673}{1016064} + \frac{5429}{1008} \eta + \frac{617}{144} \eta^2 - \sigma \right), \quad (141)$$

$$d_4 = -\frac{2355}{1462} e_0^2 f_0^{19/9} f^{-19/9}, \quad (142)$$

$$k_4 = -\frac{\mathcal{S}^2}{12} \bar{\omega}, \quad (143)$$

$$a_5 = \frac{743}{168} - \frac{33}{4} \eta, \quad (144)$$

$$b_5 = \frac{27}{5}(\beta - 4\pi), \quad (145)$$

$$c_5 = 18 \left( \frac{3058673}{1016064} - \frac{5429}{4032} \eta - \frac{617}{96} \eta^2 - \sigma \right), \quad (146)$$

$$k_5 = \frac{3\mathcal{S}^2}{56} \bar{\omega}. \quad (147)$$

## References

- [1] Supernova Search Team Collab. (A. G. Riess *et al.*), *Astrophys. J.* **607**, 665 (2004)
- [2] E. J. Copeland, M. Sami and S. Tsujikawa, *Int.J.Mod.Phys.***D15**, 1753 (2006)
- [3] Y. Fujii and K. Maeda, *The Scalar-Tensor Theory of Gravitation*, Cambridge University Press (2007)
- [4] P. J. Steinhardt and F. S. Accetta, *Phys.Rev.Lett.***64**, 2740 (1990)
- [5] C. Brans and R. H. Dicke, *Phys. Rev.* **124**, 925 (1961)
- [6] B. Bertotti, L. Iess and P. Tortora, *Nature* **425**, 374 (2003)
- [7] M. Fierz and W. Pauli, *Proc. Roy. Soc. Lond.* **A173**, 211 (1939)
- [8] G. R. Dvali, G. Gabadadze and M. Porrati, *Phys. Lett.* **B485**, 208 (2000)
- [9] K. Danzmann, *Class.Quant.Grav.***14**, 1399 (1997)
- [10] LISA web page: <http://lisa.nasa.gov/>
- [11] D. M. Eardley, *Astrophys.J.***196**, L59 (1975)
- [12] C. M. Will, *Astrophys.J.***214**, 826 (1977)
- [13] C. M. Will and H. W. Zaglauer, *Astrophys.J.***346**, 366 (1989)
- [14] C. M. Will, *Phys.Rev.***D50**, 6058 (1994)
- [15] P. D. Scharre and C. M. Will, *Phys.Rev.***D65**, 042002 (2002)
- [16] C. M. Will, and N. Yunes, *Class.Quant.Grav.***21**, 4367 (2004)
- [17] E. Berti, A. Buonanno and C. M. Will, *Phys.Rev.***D71**, 084025 (2005)
- [18] C. M. Will, *Phys. Rev.* **D57**, 2061 (1998)
- [19] P. C. Peters, *Phys.Rev.***136**, B1224 (1964)
- [20] A. Vecchio, *Phys.Rev.***D70**, 042001(2004)
- [21] R. N. Lang and S. A. Hughes, *Phys.Rev.***D74**,122001 (2006)
- [22] M. V. van der Sluys, C. Roever, A. Stroeer, N. Christensen, V. Kalogera, R. Meyer and A. Vecchio, *Astrophys.J.* **688**, L61 (2008)
- [23] M. V. van der Sluys, V. Raymond, I. Mandel, C. Rover, N. Christensen, V. Kalogera, R. Meyer and A. Vecchio, *Class.Quant.Grav.***25**, 184011 (2008)
- [24] V. Raymond, M. V. van der Sluys, I. Mandel, V. Kalogera, C. Rover and N. Christensen, *arXiv:0812.4302 [gr-qc]*
- [25] M. V. van der Sluys, I. Mandel, V. Raymond, V. Kalogera, C. Roever and N. Christensen, *arXiv:0905.1323 [gr-qc]*
- [26] T. A. Apostolatos, C. Cutler, G. J. Sussman, and K. S. Thorne, *Phys.Rev.***D49**,6274 (1994)
- [27] L. Blanchet, T. Damour, B. R. Iyer, C. M. Will and A. G. Wiseman, *Phys.Rev.Lett.***74**, 3515 (1995)
- [28] A. Stavridis, C. M. Will, *arXiv:0906.3602 [gr-qc]*
- [29] L. Barack and C. Cutler, *Phys.Rev.***D69**, 082005 (2004)
- [30] C. Cutler and E. E. Flanagan, *Phys.Rev.***D49**, 2658 (1994)

- [31] C. Cutler and J. Harms, Phys.Rev.**D73**, 042001 (2006)
- [32] A. Krolak, K. D. Kokkotas and G. Schaefer, Phys.Rev.**D52**, 2089, (1995)
- [33] C. Cutler, Phys.Rev.**D57**, 7089 (1998)
- [34] L. S. Finn, Phys.Rev.**D46**, 5236 (1992)
- [35] A. J. Farmer and E. S. Phinney, Mon.Not.Roy.Astron.Soc.**346**, 1197 (2003)
- [36] G. Nelemans, L. R. Yungelson, and S. F. Portegies Zwart, Astron and Astrophys.,**375**, 890 (2001)
- [37] S. A. Hughes, Mon.Not.Roy.Astron.Soc.**331**, 805 (2002)
- [38] W. H. Press, S. A. Teukolsky, W. T. Vetterling and B. P. Flannery, *Numerical Recipes in Fortran*, Cambridge University Press (1992)
- [39] D. A. Brown, J. Brink, H. Fang, J. R. Gair, C. Li, G. Lovelace, I. Mandel and K. S. Thorne, Phys.Rev.Lett.**99**, 201102 (2007)
- [40] M. Shibata, K. Kyutoku, T. Yamamoto and K. Taniguchi, Phys.Rev.**D79**,044030 (2009)
- [41] K. Yagi, and T. Tanaka (in preparation)
- [42] K. G. Arun and C. M. Will, arXiv:0904.1190 [gr-qc]